2014

DEVELOPMENT OF AN UNDERWATER FLAPPING FOIL TOW-TEST SYSTEM

Samuel L. Rauworth
University of Rhode Island, srauworth@my.uri.edu

DEVELOPMENT OF AN UNDERWATER FLAPPING FOIL TOW-TEST SYSTEM

BY

SAMUEL L. RAUWORTH

A THESIS SUBMITTED IN PARTIAL FULFILLMENT OF THE

REQUIREMENTS FOR THE DEGREE OF

MASTER OF SCIENCE

IN

OCEAN ENGINEERING

UNIVERSITY OF RHODE ISLAND

2014

MASTER OF SCIENCE IN OCEAN ENGINEERING THESIS

OF

SAMUEL L. RAUWORTH

APPROVED:

Thesis Committee:

Major Professor Stephen Licht

Jason Dahl

Musa Jouaneh

Nasser H. Zawia
DEAN OF THE GRADUATE SCHOOL

UNIVERSITY OF RHODE ISLAND
2014

ABSTRACT

Autonomous Underwater Vehicles (AUVs) using conventional methods of propulsion cannot operate in a dynamic environment such as the surf zone or around a reef. Bio-inspired propulsion mechanisms can provide the capabilities required to deal with the hazards of these locations. Animals such as birds, fish, and turtles use flapping foils as a means of propulsion and high maneuverability. Robotic flapping foils can be applied similarly to underwater vehicles like the AUV, Finnegan the RoboTurtle from MIT. Finnegan used four flapping foil "turtle fins" each with two degrees of freedom. One of those fins was outfitted to house force sensors which could provide instantaneous measurements of the forces acting on the foil.

The purpose of this project, is to create a system capable of testing submerged underwater flapping foils in a tow-tank using force sensors to detect fluid flow phenomena. The force sensors had to be tested, installed, and calibrated so that they measured the forces about the desired axes. A method of attaching the fins to the towing carriage had to be devised and built out of aluminum. This attachment had to be sturdy due to dynamic loading and life expectancy for future use, streamlined where it would be submerged, and user friendly. The attachment also had to be able to adjust the depth of the fin. A data acquisition system was setup to record and transfer the force sensor measurements and foil positioning data from the towed flapping foil to the computer station. Tests were run to compare to past data in an effort to validate the testing system. The system can collect valid data currently, but improvements are necessary to achieve the desired functionality.

ACKNOWLEDGMENTS

I want to thank my advisor Stephen Licht for his guidance and support throughout every facet of this project. Thanks to Matthew Perkins for his countless hours selflessly helping my progress. I also want to thank William Snyder, Fred Pease, Robin Freeland, and of course Gail Paolino. You all made significant contributions necessary to the success of this thesis.

Finally, I can never thank my parents enough for what they've done and what they've provided for me. Thank you dad, Michael Rauworth, for continually reinforcing my interest in engineering. Thank you mom, Nancy Cantelmo, for helping me keep my head above the water when I need it most.

TABLE OF CONTENTS

LIST OF TABLES

TABLE PAGE

LIST OF FIGURES

CHAPTER 1

INTRODUCTION

Motivation

Biologically inspired engineering offers boundless possible technological advances in underwater vehicle design. There is still an extraordinary amount to learn from the world's oceans and the sea-life that inhabit them. The flapping foils of batoid fish and turtles can produce propulsion and maneuverability unlike any propeller-driven system. Sensing in the way fish do with lateral lines and sea mammals do with whiskers could allow a vehicle to navigate in a dynamic environment, or even utilize benefits of certain fluid flow phenomena. Mimicking these natural designs is often a complex problem.

The purpose of this project is to provide a multi-functional testing platform to advance the capabilities of underwater vehicles using flapping foils.

Underwater flapping foil vehicles have potential to greatly expand the operating space of standard propeller-driven vehicle. This project is a component of the research done in the Robotics for Complex Underwater Environments Lab (R-CUE). Dynamic environments such as the surf zone, around reefs and wrecks, and also rivers are currently out of bounds to autonomous underwater vehicles (AUVs). Operating near the seafloor is dangerous to vehicles unequipped to handle the different fluid flow effects that exist in that region. Force sensors installed in a flapping foil can give instantaneous estimates of the forces acting on the foil during motion. These forces can be used to quantify properties such as thrust, lift, and efficiency of the foil.

They can potentially be used to detect the presence of ground, walls, and the free surface.

Thesis Contents

Chapter 2 is a review of the literature pertaining to the flapping foils used in the project. It provides background information necessary to understand the foundations this project was built on. The Chapter 3 methodology explains the design, building, and testing of the major thesis components. These include the force sensors, carriage attachment, and data acquisition system. Chapter 4 includes the results of from force sensor calibration to the full system towed experiments. That section explores the trends and comparisons to past data. Chapter 5 provides details of modifications that will be made to the system, while also analyzing the existing sources of error. The future work is outlined in Chapter 6, which describes experiments that will be run with the current system, and testing of other projects currently in the research and design phase. Finally, the summary and conclusions brings all the basic findings together while providing a succinct statement of the project outcome.

CHAPTER 2

REVIEW OF LITERATURE

The flapping foils used for this project come directly from Finnegan the RoboTurtle. Finnegan is an AUV developed at MIT which uses four flapping foils for all motion. The abilities of the flapping foils on this vehicle include propulsion, station keeping, high maneuverability, high turning speed, and low turning radii. Though the vehicle was large and weighed about 500lbs out of water, the flapping foils made it capable of advanced maneuvers compared to that of standard propeller driven vehicles.

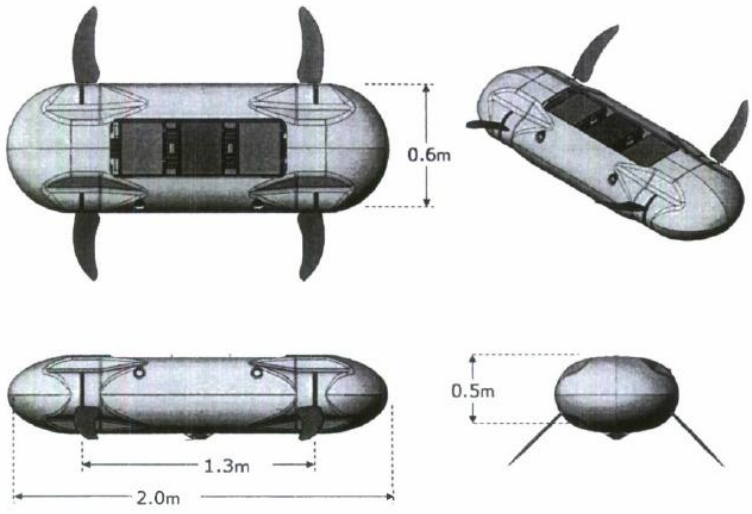

Figure 1: Finnegan the RoboTurtle

The four flapping foils could achieve forward motion of 1.2 m/s, with each fin producing a maximum of 100N of lift with a mean thrust of 22N [Polidoro, 2003]. The solid model of one of the flapping foil systems is shown in Figure 4.

Design, construction, and testing of these self-contained flapping foil systems is detailed in [Polidoro, 2003]. In that thesis, the system was towed in a tank with similar dimensions to the URI tow-tank. The MIT tank is 30m long, 2.5m wide, and 1.1m deep, compared to the URI tank which is 30m long, 3.5m wide, and 2m deep. The fin used was a standard NACA 0012 airfoil with a rectangular planform. There were four span lengths used of 0.3m, 0.4m, 0.5m, and 0.6m. Data provided includes thrust coefficient contours and time sequence lift and thrust data.

Data was collected in the MIT Tow-Tank using a six-axis strain gauge dynamometer which was mounted between the towing rig and the flapping foil. Force measurements were made externally to the system, at a sampling rate of 100 Hz. The experiments were towed at 0.5 m/s with just the fin submerged. The Reynolds number during testing was about 50,000. Sensor calibration, testing procedure, and post processing from that thesis created a basis for the methods used in this project.

[Licht, 2008] described the creation of Finnegan the RoboTurtle from researching the swimming of an actual sea turtle to full-scale tests of the AUV in a pool. Finnegan used fins with a planform shape similar to a turtle and those same fins were used in this project. Licht gives insight on the wake formations from these flapping foils when they are fully submerged. Finnegan provides a direct link between testing the foils and their applied capabilities on a underwater vehicle. The maneuverability and other motion capabilities exhibited by Finnegan are highly dynamic compared to propeller driven vehicles. Finnegan was equipped with a six-axis accelerometer, four narrow beam altimeters, a pressure sensor for depth measurement, and a downward facing doppler-velocity logger. These sensors provide

adequate knowledge of the vehicle's location in the water, however there are no methods to instantaneously sense the fluid flow around the vehicle or the flapping foils.

[Techet, 2008] investigated thrust coefficient contours over a range of Strouhal numbers and maximum angles of attack using a similar testing system. The contour plot from that paper with a heave to chord ratio ($\frac{h_o}{c}$) of 1.5 provides the data that this project seeks to replicate to validate the new test system (Figure 2). Each red dot in that plot represents one test run with the corresponding Strouhal number and maximum angle of attack (α_{max}). Thus, there were at least 28 tests performed. The shape of the fin used resembles a combination of a turtle fin like Finnegan used, and the rectangular planform from the Polidoro testing. A important difference is that the span and chord lengths were respectively 61.5% and 55% of the lengths used in this project.

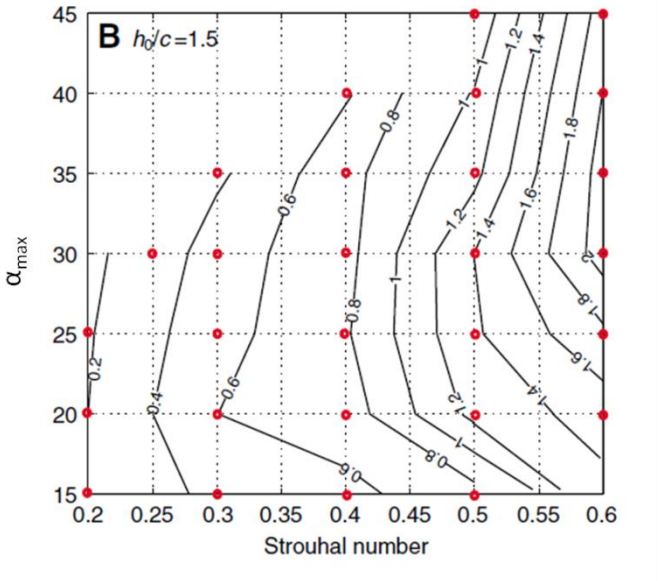

Figure 2: Thrust Coefficient Contours (Techet)

Techet performed experiments in a flow tank where water was forced past the flapping foil instead of the foil being towed through stationary water. Forces were again measured with a six-axis strain gauge sensor, a torque sensor was used to measure roll shaft input power, and potentiometers mounted to each shaft gave additional position data. The author notes that the location of the center of pressure on the foil varies while flapping, but to keep consistent with propeller notations a position of 70% of the span length from foil root to tip is used for nondimensional calculations. The Reynolds number was varied between 27,000 and 55,000.

[Licht & Dahl, 2013] used a heaving and pitching NACA-0012 airfoil in a small tow-tank to examine ground-effect on flapping foils. The foil aspect ratio (AR) or the ratio of chord to span length was ~6.4 compared to the AR of 4 used in this project. The airfoil used in their study is an extruded aluminum foil with a rectangular planform. Force sensing was done with a six-axis dynamometer. The foil heaves and pitches to flap near a solid wall of the tank. The wall was adjustable such that they could test different distances and vary the $\frac{h_{ground}}{c}$ ratio. Their findings show the mean generated lift while the fin moves towards the wall changes significantly with relation to distance from the wall. Also, they found an 18% difference in peak magnitude of instantaneous lift in downstroke vs. upstroke. That variation is instantaneously visible and therefore does not need to be compared to past data. This would allow a vehicle to potentially use ground-effect to benefit operation in real time.

CHAPTER 3

METHODOLGY

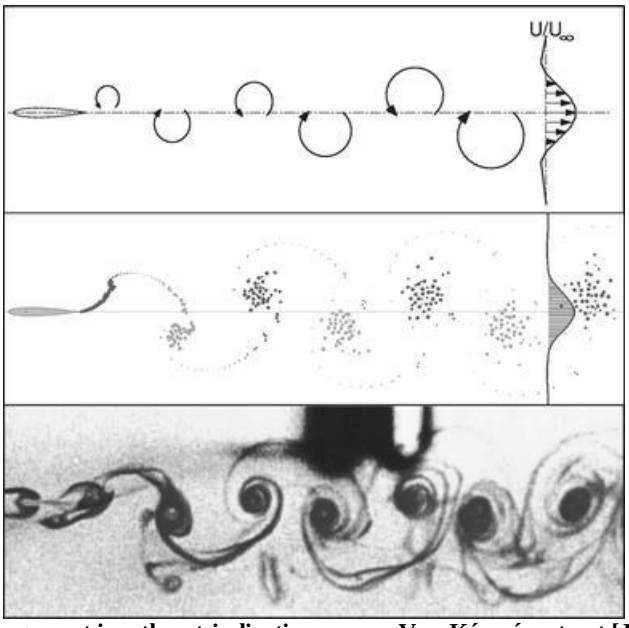

Figure 3: Vortex arrangement in a thrust-indicative reverse Von-Kármán street [Jones & Platzer 2009]

3. 1 Foil Kinematics

Flapping foils create propulsion by generating a wake pattern of vortices that act like a jet to provide thrust. This pattern is called a reverse Von-Kármán street (Figure 3). The foils can also be used to create lift and drag and be used as control surfaces to maneuver the vehicle. Each of the four foil systems has two degrees of freedom referred to as pitch θ and roll ϕ. They each consist of the same two cylinder design with the roll motor, control card, amplifier, and power input in the large main cylinder, and the pitch motor components in the pitch cylinder. The roll motor rotates the entire pitch cylinder about the Y-axis, and the pitch motor rotates the turtle-fin foil about the X-axis as shown in Figure 4.

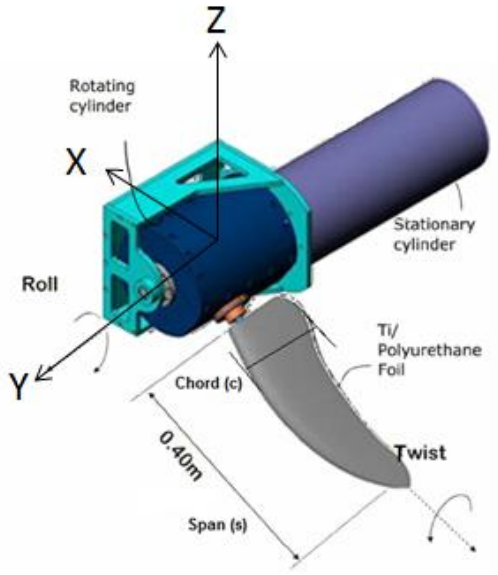

Figure 4: Flapping Foil System

The kinematics and equations for each parameter used are the same as those in the theses of Victor Polidoro and Stephen Licht [1,2]. The most important of these are explained below, paraphrased from those theses.

The equation for the roll position of the fin is given by:

$$\phi(t) = \phi_0 \sin(\omega t)$$

The equation for pitch position of the fin is:

$$\theta(t) = \theta_0 \cos(\omega t)$$

Where $\phi_0$is the roll amplitude in radians, $\theta_0$is the pitch amplitude in radians, ω is the frequency of foil motion in radians per second, and *t* is time.

This rolling and pitching motion causes a varying angle of attack with two components as opposed to a static foil like those on an airplane. The first component is the instantaneous pitch angle, and the second is the angle of incoming fluid based on the ratio of the pitch and roll velocities. The total angle of attack is not constant over the span of the foil, but a location was chosen which corresponds to an assumed

effective center of hydrodynamic force. This location is 70% of the span length from the root of the foil ($r_{0.7}$). The root of the foil is the end of the foil that is closest to the roll-axis.

$$r_{0.7} = r_0 + 0.7s$$

Where r_0 is the distance from the center of the roll axis to the root of the foil, and *s* is the span length.

Using that distance, the angle of attack is given by:

$$\alpha(t) = -\arctan\left(\frac{\omega r_{0.7}\phi_0 \cos(\omega t)}{U}\right) + \theta_0 \cos(wt)$$

[Techet 2008] showed the maximum angle of attack (α_{max}), affects lift, thrust, and wake structure. The data comparison done later maps mean thrust coefficients ($\overline{C_t}$) using α_{max} and the Strouhal number as desired parameters. The desired Strouhal number defines the roll amplitude used, which leaves the pitch amplitude as the only unknown for the above angle of attack formula.

The Strouhal number (St) provides an important ratio to characterize the vortex pattern as it relates the velocity of the fluid or vehicle (U) to the frequency and size of each generated vortex. It therefore "describes the geometric spacing of the vortices in the wake." [1] St is defined below in the formula with *U*, flapping frequency (f) and the arc length of the flap. The arc length uses the $r_{0.7}$ value as well as the roll amplitude ($2r_{0.7}\phi_0$).

$$St = \frac{2r_{0.7}\phi_0 f}{U}$$

The last nondimensional ratio of significance relates amplitude of the heave motion to the chord of the foil:

$$\frac{heave\ amplitude}{chord\ length} = \frac{h_{0.7}}{c}$$

Where the heave motion is defined by:

$$h_{0.7} = r_{0.7}\phi_0$$

3.2 Force Sensing

This project makes use of two piezoelectric force sensors mounted inside the pitch cylinder of a flapping foil mechanism. Installing the sensors in the device should produce direct measurements of the forces acting on the fin. With the sensors in the pitch cylinder, the whole system can be submerged which eliminates some inertial effects and body drag does not need to be subtracted. One of the four foil systems from Finnegan the RoboTurtle [Licht, 2008] was already outfitted with special mounting plates needed to mount the sensors. The plate design was modified as described in the *Installation Design* section.

Sensor Details

Two Type 9602 sensors from Kistler were installed between aluminum plates inside the pitch cylinder. These sensors have integrated amplifiers, which makes the body larger, but removes the necessity for expensive external amplifiers and also reduces the system's complexity. Each sensor measures forces in three directions, Fx, Fy, and Fz. As shown in Figure 5, they have a donut shape that houses the piezoelectric ceramics that detect the forces. For this to work, each sensor must be preloaded by a bolt through that donut hole which means a constant force must be applied as a reference. The bolt must also have an elastically deformable plastic sleeve to make sure the forces delivered are not distorted by space between the bolt and sensing surfaces.

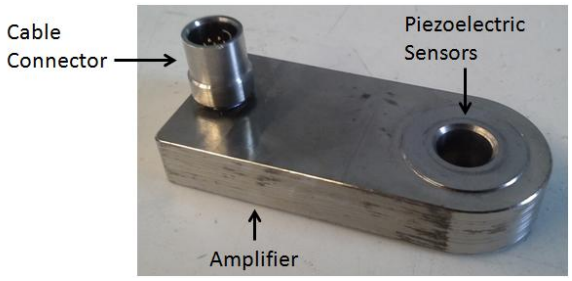

Figure 5: Force Sensor

The full specifications can be found in Appendix 1, but the most important ones are noted here. Each sensor outputs analog voltages between +/-5V, nominally proportional to forces in the principle directions, which can be converted to forces after calibration. The measuring range for the axial direction is -5kN to 5kN, and for the other two directions is -2.5kN to 2.5kN. The forces expected from testing are a safe factor of 100 less than those limits. With the integrated amplifier, each sensor is still small enough to fit in the cramped space of the pitch cylinder. Communication comes by way of Cat 5 cable using 7 of the 8 conductors.

Installation Design

The pitch cylinder had a deeper cavity milled out of the Delrin to make space for the two aluminum plates that sandwich the force sensors. The plates provide the necessary preloading when bolted together. The bottom plate is bolted to the floor of the pitch cylinder cavity, while the motor components are mounted to the top plate. This means that the bolts through the forces sensors that hold both plates together are the only way forces are translated through the system. The pitch shaft leads out of the cylinder to the fin.

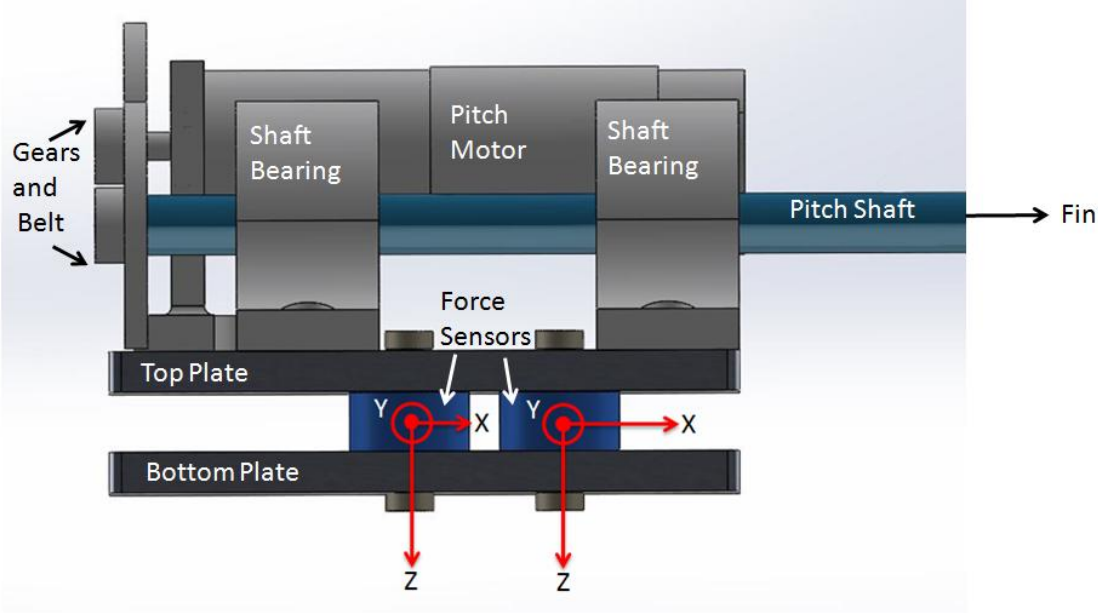

Figure 6: Force Sensor Locations (front view)

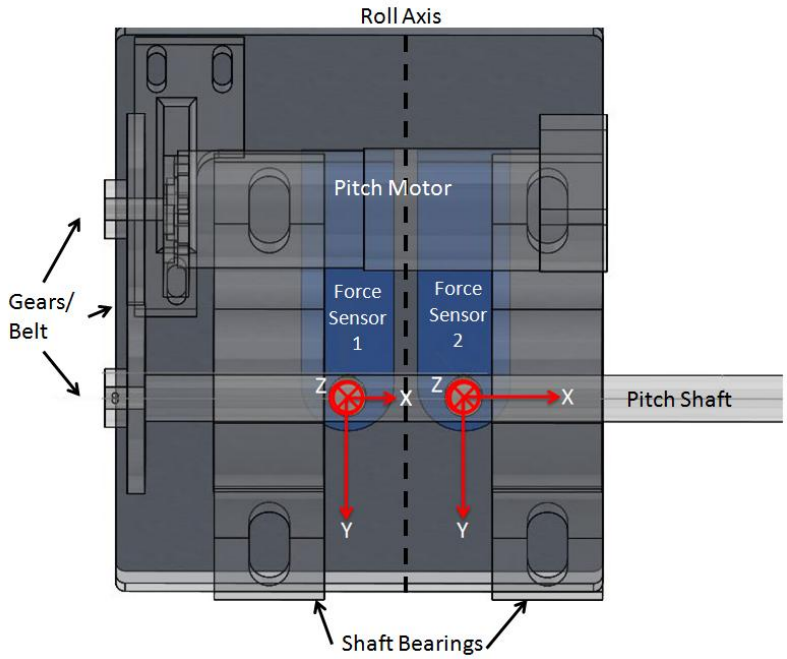

Figure 7: Force Sensor Locations (top view)

The locations of the two sensors (shown above) were determined based on the desired forces to measure, and available space around the other components. Two holes were drilled through both aluminum plates in-line with the pitch shaft. These

holes were for the bolts going through the sensors. Two larger holes were drilled through the top plate for the communication cables to extend through.

The communication cables that came with the sensors had short Cat 5 tails which needed to be extended about 2m and terminated and the surface with RJ-45 connectors. Since the previous outputs of the pitch cylinder were wet mateable connectors with no unused pins, one of the connectors was removed and a new waterproof outlet was designed to take the two sensor Cat 5 cables along with the power and ground cables that go to the roll cylinder. The first choice was to just make a large enough hole and epoxy it closed, but this proved very difficult to keep waterproof since moving the cables deformed the epoxy. The hole was then threaded and a pipe nipple was screwed in with an o-ring to create a solid capsule to shield the epoxy from outside influences. This method proved effective, though it was still not waterproof as the epoxy used was very rigid. After a flexible epoxy replaced the rigid one, the connection held a vacuum, that is to say it was waterproof.

Calibration

The calibration of the force sensors involved designing and fabricating a method to hang test-weights applied to all three axes, collecting data with multiple weights at different distances from the sensors, and processing the data to output calibration matrices. A simple pulley system was created to hang weights on a line attached to different notches (indicated with red arrows) on one of the extra fins as shown in Figure 9.

Figure 8: Pulley System

The pulley system proved unable to produce accurate results which can likely be credited to friction of the line and pulley. The next method chosen was to hang the weights directly from the notches with the fin angled perpendicular to the ground. The body of the flapping foil was rotated so that the forces were applied in the correct axes. This method allows independent variation of forces and moments. Therefore, each moment measured was a direct result of a force applied in the correct direction at the distance each notch was from the sensor in question.

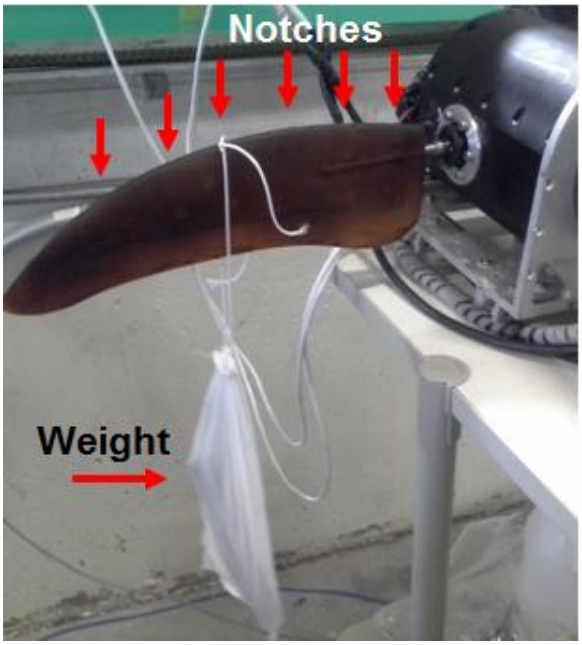

Figure 9: Weights Hanging from Notches At Red Arrows

The weights used either had rope tied around them for hanging or were placed in small bags. The weights were 0.726kg, 1.725kg, and 2.269kg. Those values account for the weight of the bags and other hardware used in the system. The fin used has 6 notches spaced 0.04m apart, and 3 weights were hung from each notch. The data was collected using the full data acquisition system used for experiments. Each weight was given 10 seconds to hang and 10 seconds before and after hanging to let the sensors settle. The weights were labeled with letters and hung in the same order every time for testing consistency and repeatability. Once all data was collected, it was processed using Matlab to find the force sensor sensitivities (see *4.1 Calibration*).

3.3 Carriage Attachment

The tank and mobile tow-carriage in the Sheets building on the Bay Campus of URI have been used for towing models and instruments in the past. However, no structure has previously existed that would provide a sturdy, and modular connection of a flapping foil to the carriage. Size and weight of the towing package contributed

greatly to the design constraints. The importance of this structure is not solely for the flapping foil, but it is also expected to serve the needs of future towed mechanisms.

Design Constraints

The Carriage Attachment (CA) was designed originally for Ground-Effect experiments. Those experiments required the ability to tow a flapping foil and accessories at varied distances from the bottom. This implies that either the vertically-adjustable bottom sections of the tank (referred to as the beach) would have to be used, or the CA height must be modular. It was much more practical to make the CA modular than to go through the extensive beach adjustment process. The CA also had to be streamlined under the waterline so as not to add increased drag that might bend the attachment or hinder the movement of the carriage, or generate significant vortex induced vibrations.

The bulk of the towing package would itself require quite a rugged towing apparatus, but flapping also produces lift and thrust forces that translate through the structure. The three direction linear force constraint of the CA was to be strong enough to withstand up to 250N in each direction. This number comes from the conservative combination of the weight of what was towed (~170N) and a maximum of about 60N of fin-produced forces like lift and thrust [Polidoro, 2003]. Due to the static and dynamic loads, the strength of the structure was dependent not only on configuration, but also on the materials chosen. The materials had to be corrosion resistant over long periods of submersion, able to endure linear and torque forces, and still be light enough not to restrict the carriage movement or the ability to install and uninstall the structure.

Design Procedure

The first step taken was to create a solid model of the carriage and CA so it would fit and make use of the strength offered by the carriage beams. The use of 80/20 aluminum extrusions and connectors was an early choice for the CA. 80/20 is a highly adaptive building material coined “The Industrial Erector Set”(www.8020.net). The solid models of most 80/20 pieces are available to download for free and allowed easy construction of a system model with the carriage.

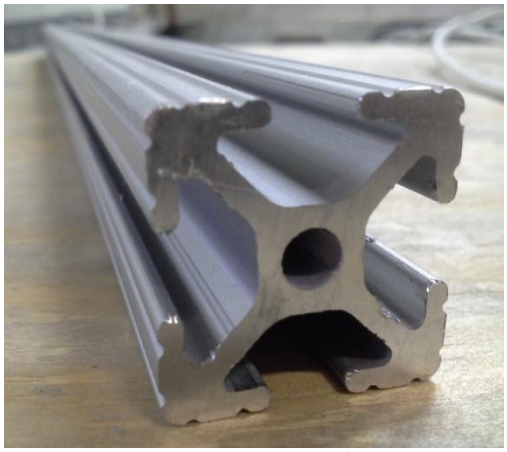

Figure 10: 80/20 Profile

A truss structure was selected to bridge the spacing of two middle beams. This would provide a strong foundation rigidly attached to the beams to stop sliding movement caused by accelerations of the carriage and the momentum of the structure. The sections of extruded 80/20 and connectors were purchased online from multiple distributors including McMaster Carr, iAutomation, and Air Inc.

The truss is comprised of two sections. The top section provides the attachment to the carriage, resistance to applied forces, and is designed for the towing package load with or without the bottom section. The bottom section, referred to as "the cube" is a spacer to place the towing package closer to the bottom of the tank. The cube is a 0.4m extension which is the same height as the towing package when it uses the

pontoon. The equivalent lengths means the towing package can be adjusted 1 unit body-height up or down with relative ease. The twelve sections that shape the cube are each 1ft long with $1in^3$ corner connectors. There are also diagonal bracing pieces on four sides, and cross bracers on the top and bottom. The cube and the top section connect using the 80/20 4-hole joining plates. At the bottom of both the cube and the top section exists the proper hardware and beams to connect to the mast section.

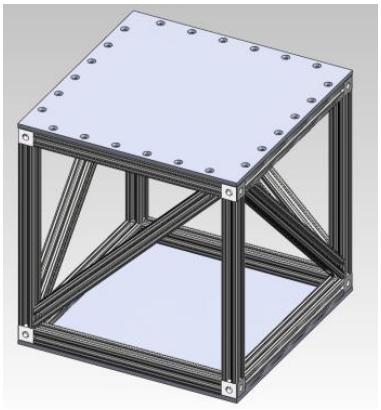

Figure 11: Extension Cube

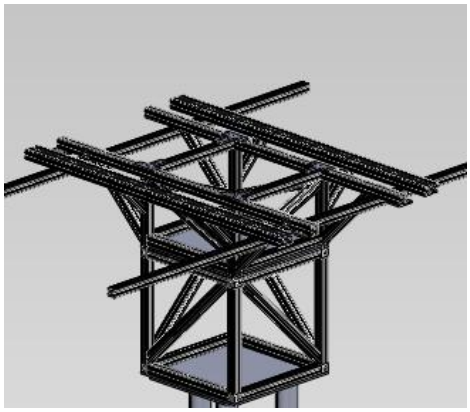

Figure 12: Top Truss With Cube

The mast section is the part of the CA that is partially submerged during testing and is therefore comprised of streamlined lengths of masts from a small sail boat. The material is extruded and anodized 6063-T6 aluminum. There are three pieces, each 36in (~0.9m) in length, and were cut from two 8ft (~2.4m) sections of Kenyon Mast Section B from Rig-Rigrite, Inc. (www.rigrite.com). The B-Section mast

was chosen for a variety of reasons. The planform shape is the most fore-aft symmetrical of the sections available which allows for similar results while towing in both possible directions. The wall thickness and outer dimensions of the B-Section were determined as adequate with the 36in length when beam deflections and torsion was calculated. Those calculations were done with the previously noted forces applied by the tow package. Finally, the interior space was large enough to act as a cable conduit for the communication and power cables spanning from towing package to surface.

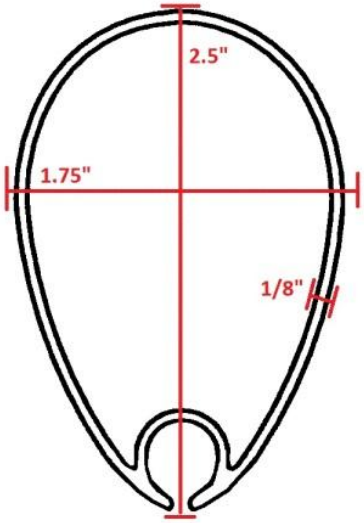

Figure 13: Mast Profile (rigrite.com)

The reasons for three small mast sections instead of a single larger one are based on the expected applied forces and availability considering the required size disparity i.e. one mast would have to be much larger than three to produce the same strength. The three masts are arranged in a triangular orientation between two plates of 6061-T6 Aluminum. The triangle shape gives the structure great capacity to resist deformation. For symmetry, an acute triangle was used with the forward point being the standard forward direction of travel. The dimensions of this triangle were chosen

based on both the dimensions of the connection to the 80/20 sections, and on a fluid flow analysis of the interactions each mast has on each other. The fluid flow analysis was done using SolidWorks Flow Simulation with freshwater modeled from speeds of 0.25m/s up to 1m/s. The scale of the triangle was expanded until there were no visible interacting effects on the flow around each mast coming from the other masts.

Finally, the total CA is attached to the towing package by sliding the flapping foil attachment onto two mounted pieces of 80/20, and elastic polyurethane cords hook from the pontoon to plastic I-bolts on the bottom aluminum plate. The flapping foil is held in place laterally by two pairs of the standard 80/20 lock nuts.

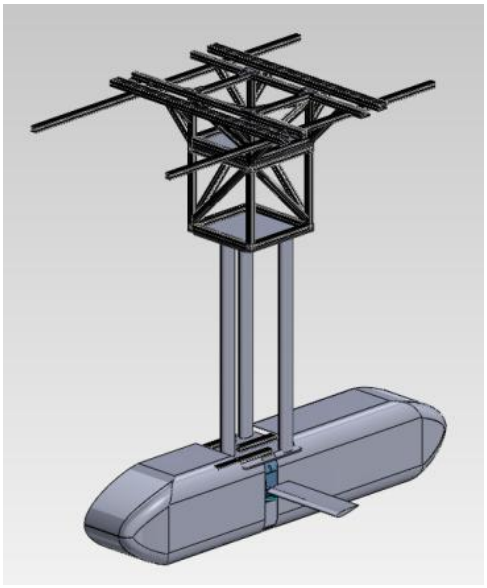

Figure 14: Full Carriage Attachment Model

Build Parameters

Stock 80/20 extrusions were cut to the desired lengths and angles. Once all cuts had been made, the proper connecting plates and bolts (Figure 15) were applied to put the upper truss structure together matching the model. All of the load-bearing 90^{o} connections use an “anchor” which was counter sunk into the 80/20 on two sides to create a high-strength locked connection (see Figure 15). All pieces are aligned within

1^{o} of their intended angle and the horizontal pieces were all leveled. The truss can either connect to the cube or the mast section.

Figure 15: Anchors vs. Bolts and Plate

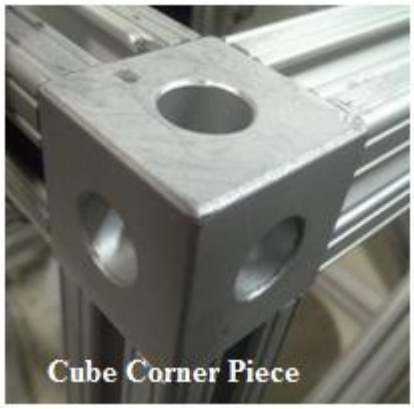

Figure 16: Cube Corner Piece

The cube used 3-direction cubic connectors as shown in Figure 16. Each of the twelve pieces of 80/20 that make up the basic cube had to have the internal shaft threaded at both ends for the screw to connect the pieces to the connectors. This creates another strong 90^{o} joint similar to using anchors. All bolted components of the cube were adjusted to make sure the top and bottom frames were level in the same way as the previously truss. To connect the cube to the truss, four aluminum plates, each with four holes, are screwed into the bottom truss frame and the tope cube frame as indicated in Figure 17.

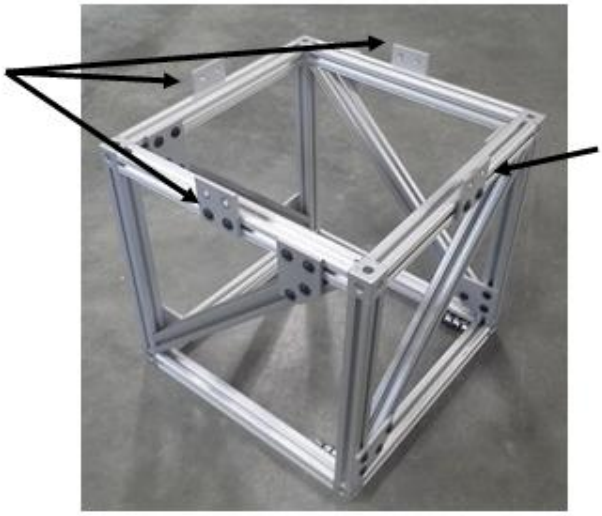

Figure 17: Cube With Attachment Plates

This joining method is similar to the way the top plate of the mast section is attached. Holes were drilled in the top plate, and the standard 80/20 bolt and nut hardware is used to screw the mast section and two parallel pieces of 80/20 together. Those two parallel pieces are fixed to the bottom of the truss or the cube via anchors.

Figure 18: Carriage Attachment Structure

Fastening each section together using bolts is not a very quick method which means modifying the CA configuration is time consuming. However, the structure is

very sturdy compared to a quick-release design, and the time is on the order of minutes which is acceptable given the total time of average experimental use. There are no moving parts to fail, all components are inexpensive, and they come from the same manufacturer which makes them easily replaceable. The mast section was cut and welded at a local machine shop, Fabri-Tec Engineering (Wakefield, RI) based on the generated design drawings.

Installation/Removal Method

At the time of the original installation design, the tow-tank carriage had large steel beams on top occupying a lot of space. This made it necessary to bring the CA up from below the carriage, maneuver it in place, and then bolt it to the carriage. The whole ordeal had to be done with at least one person standing in the water of the tow-tank for a significant amount of time. Four bolts were threaded facing up through the carriage beams upon which the CA would slide down into place and be fastened down with nuts and lock washers. In order to restrict any movement caused by hole-to-bolt size differences, the positioning of the bolts and corresponding holes was very tight. The CA could slide down the bolts with some fuss, but could not be removed without removing most of the bolts. There were a number of flaws that made bolt removal taxing of time and physical strength including: the bolts were threaded into the C-beams from below, there was restricted spatial access to the bolt head, and the bolts had a smooth cap instead of a socket hole. Time for installation and breakdown would sometimes exceed an hour for each.

To remedy the bolt issue, three of the bolts were removed and replaced with socket-head bolts that were screwed in from above the carriage. The one remaining original bolt was left as a guide to slide the CA down. This resulted in total bolting

and unbolting times of less than 5 minutes with use of a hand drill and the proper bit. Similarly, the time and method to get the CA to the bolting location was drastically altered. All intruding steel components were removed from the top of the carriage which allowed the CA to be raised up via winch, and lowered through the top of the carriage. This method not only reduced the total installation time from hours to around 20 minutes, but it also kept all participating parties dry the entire time. With some extra time and physical labor the installation process is doable by a single operator, though it is highly preferable to have two.

Performance Analysis

With the most updated installation technique, no problems have arisen in relation to the bolting throughout testing. There are also no visible vibrations or deformations under testing loads. All connections have held up and the structure has remained flush in the three axes which is indicative of positive integrity. Fluid flow around the mast section in both directions seems concurrent with the models implying similar forces applied due to the symmetrical and streamlined profile. Significant corrosion has not been detected. The CA has been stored hanging as well as braced against steel beams and concrete putting stress on many of the different members. Even with the weight, and sometimes chaotic jostling that comes with a single user, the structure remains solid.

3.4 Data Acquisition System

Table 1: Complete Data Network Outline

Flapping Foil	Towing Carriage	Computer

• Two Piezoelectric Force Sensors (Kistler Type 9602)
• 1 Cat5 cable per sensor to surface
• Galil Control Card with Ethernet communication
	• National Instruments Chassis
	• 68 I/O DAQ board
	• LDM 42 Laser Distance and Timing
	• 2 Channel Power Source
	• Fiber optic cable to Computer
		• Galil Tools program controls flapping foil
		• LabView records
		  • Force sensor data
		  • Foil motion data
		  • Laser distance and timing
		• Matlab for data analysis

The Data Acquisition system (DAQ) consists of an I/O board, a processing chassis, a laser distance measurement sensor, fiber-optic communication, and computer programs. The foil mechanism and force sensors are powered by a BK Precision 1673 triple output power supply. The system allows analog signals from the force sensors to be sent digitally from the flapping foil in the water to the land-based computer where they can be visualized and recorded. The boards and processing box are mounted to a wooden platform on top of the tow carriage. The fiber-optic cable is run from that platform, along the carriage power lines, and around the tow tank to the computer. This section will explore in-depth each component, how everything is configured, and the total communication paths.

Components

The first component in the connected system is the data acquisition board mounted to the carriage platform. This board is an NI SCB-68A from National Instruments with 68 I/O channels. There are four inputs from each force sensor that

attach to the board which are the three direction force voltages (Fx, Fy, Fz) and ground. The cable at the top leads to the chassis. There are three other identical boards that would allow for a large expansion of the DAQ both on the carriage platform and on the land-based system. Each chassis only has two inputs for these boards currently, but that can be expanded if desired.

The laser range finder is used for experiment timing. This is a LDM 42 A from ASTECH with a class 2 laser, up to 100m range, and 2mm measuring accuracy. Since both channels on the power source are taken, the programmable power from the chassis is used. Communication is via RS-232 from laser to chassis. The laser sits on the carriage platform and aims towards the wave maker, terminating at a white target on the wall for favorable reflectivity. While the laser distance output can be differentiated to produce instantaneous velocity, the average is used for this project as the carriage is controlled to a constant velocity. Therefore, even though distance can be measured at either 10hz or 50hz, only the first and last distance and time measurements taken during testing are used.

Figure 19: LDM-42

The next component in the data path is a NI PXIe-1082 chassis mounted on the carriage platform. It can accept the I/O from two boards, four RS-232 ports with female RJ-45 inputs, two gigabit Ethernet input ports, and there is also a digitally controlled power supply. Each of the different types of inputs and outputs come from individual I/O modules which fit in 8 interchangeable slots on the box. Included in the

image below are the NI PXI-4110 Programmable DC Power Supply, NI PXI-8432/4 RS232 Isolated, NI PXI-6225 M Series Multifunction DAQ, NI 8234 Dual Gb Ethernet, and NI PXIe-9375 MXI-Express X4. This means the DAQ can be set up to provide data acquisition capabilities over a large variety of experimental configurations. Figure 20 shows the current configuration.

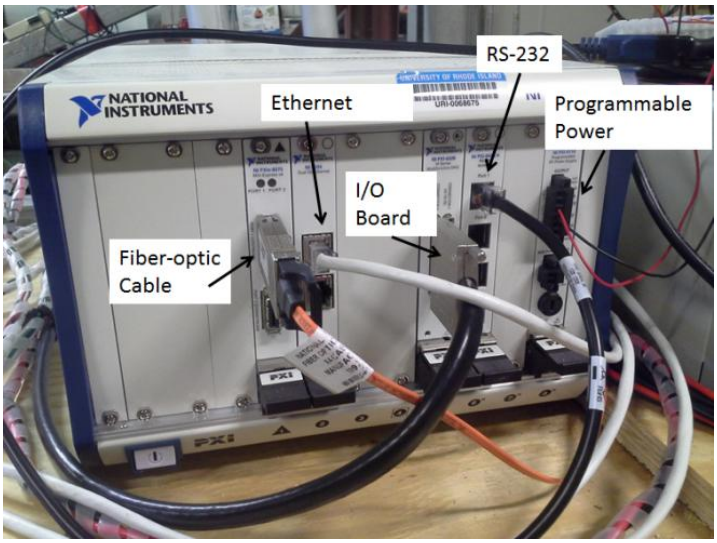

Figure 20: Chassis Front Panel Connections

The chassis communicates to the land-based computer via the fiber-optic cable. There is 100m of this cable available, though much of it is coiled up in its current installation. The cable sends the digital input signals to the computer where it is received and interpreted using the following programs. National Instruments provides proprietary software which allows the user to see all connections from multiple chasses, test the connections, and view the inputs being received. Galil Tools Lite is a free program used to control the flapping foil. A custom LabView2012 VI was used to monitor and record the force sensor outputs as well as poll the control card for instantaneous velocity, position, and torque estimates.

Configuration

The components housed on the carriage platform are mounted in ways to avoid outside objects during towing, and to resist movement caused by carriage direction changes. Both the chassis and power source sit between pieces of wood drilled into the platform that are large enough to stop any slipping movement, but small enough and out of the way such that all buttons and inputs are free. The I/O board has 3 holes to slides onto screws so it can be durably installed and easily uninstalled. The LMD 42 is also screwed to the platform.

The fiber-optic cable used has an 8lb tension strength so it runs through PVC tubing whenever possible to remove exposure to the hazards of machinery and human traffic. To connect from the carriage to the computers, the cable is zip-tied in loops to the carriage power cable. Both cables can travel the length of the tow tank and are pulled by the carriage, therefore there are wires connecting each loop that are shorter than the looped distance to take the tension of pulling the cable. The fiber-optic cable has even more extra length per loop to make sure it is never strained to the breaking point. The cable is eventually terminated at the land-based computers into a mounted NI PXIe-PCIe8375 card.

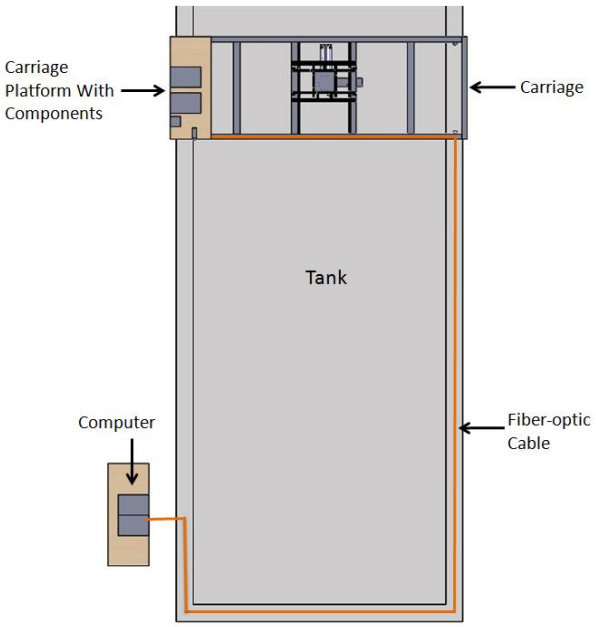

Figure 21: DAQ Configuration

Figure 21 shows the current setup of the DAQ. This is a birds-eye view of a solid model. The carriage platform is shown at the top left with components installed. The path of the fiber-optic cable is traced around the rim of the tank, and terminates at the computer. Figure 22 below shows a profile view of the carriage section of this model.

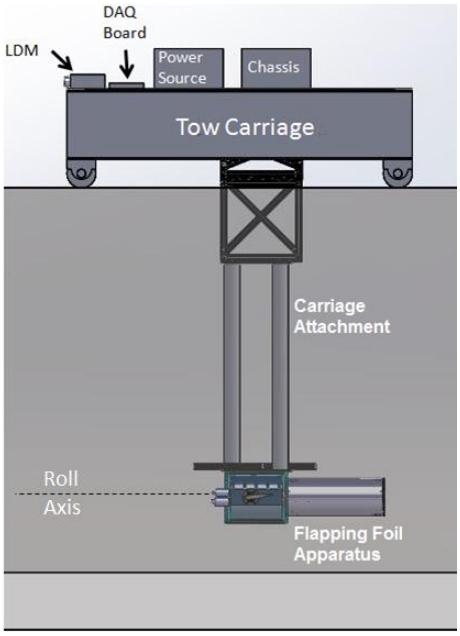

Figure 22: Carriage Mounted DAQ Components

CHAPTER 4

RESULTS

4.1 Calibration

The force sensors were calibrated in-situ by hanging 3 known weights from 6 notches in one of the fins. Each notch is 4cm apart starting from 0.175m from the roll axis. The weights were hung with the apparatus oriented to apply a force in the Z-direction, and then reoriented for the Y-direction. To find the resultant force acting on each sensor with each weight, the following equations were solved.

$$\sum F = F_1 + F_2 + F_3 = 0$$

$$\sum M_2 = F_1 * l_c + F_3 * l_x = 0$$

These equations correspond to the diagram below.

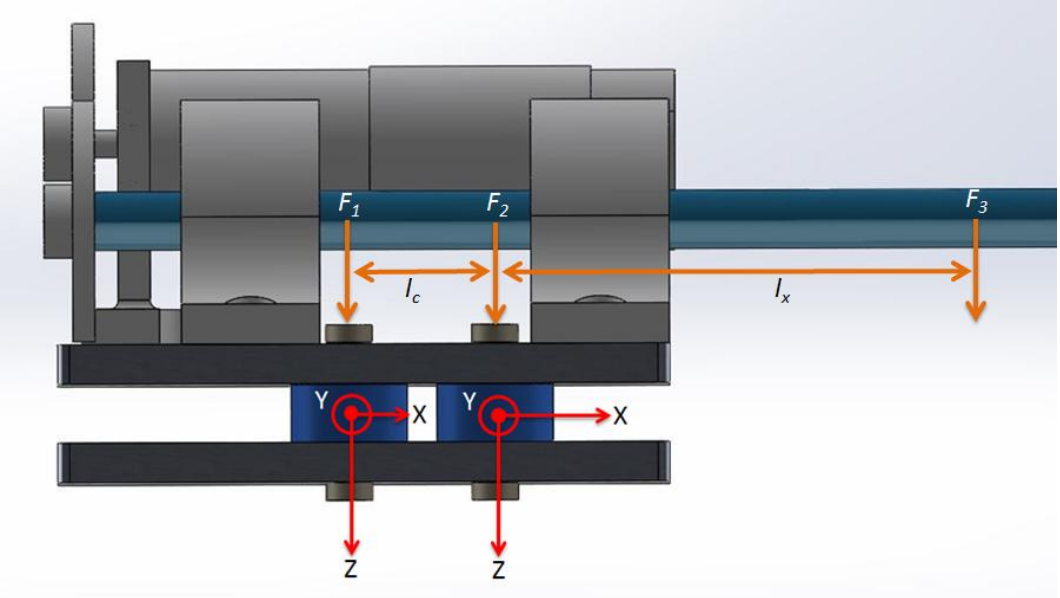

Figure 23: Calibration Forces Diagram

F_1, F_2, and F_3 are the forces acting at the 2 force sensors and on the foil respectively. "l_c" is the constant length between the force sensors, and "l_x" is the varying length between the force on the foil and Sensor 2.

These calibration tests create plots of the voltage measurements from weights hung in one direction at different distances. The example below shows weights hung in the Z-direction.

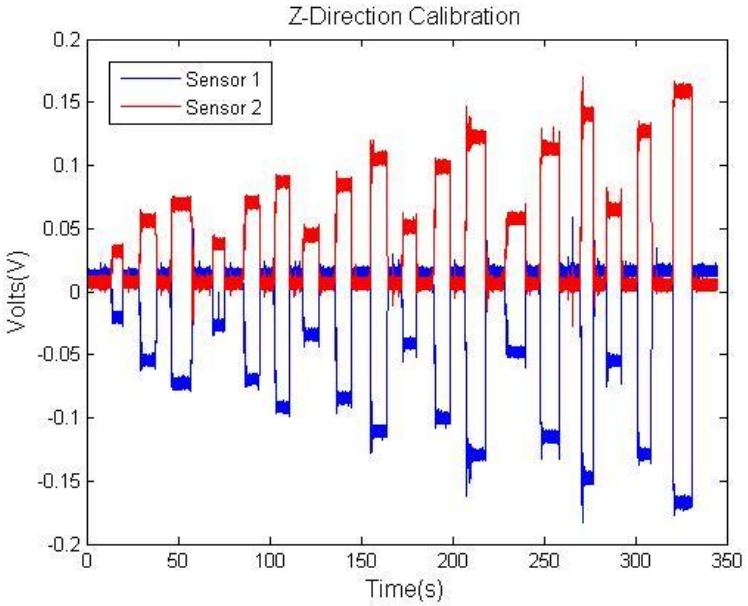

Figure 24: Force Sensor Output During Calibration

Each weight was hung for at least 10 seconds to allow for removal of the static offset and linear drift at the sensor. These 10 seconds of an applied force are represented by each voltage plateau. The average value of each plateau is taken as the single voltage output value that correlates to that applied force. A Matlab program used to organize this data allows the user to manually select the beginning and end times of each plateau. In the figures 25-28, those values in volts are plotted on the y-axis against their corresponding resultant forces on the x-axis to visualize how linear the fit is.

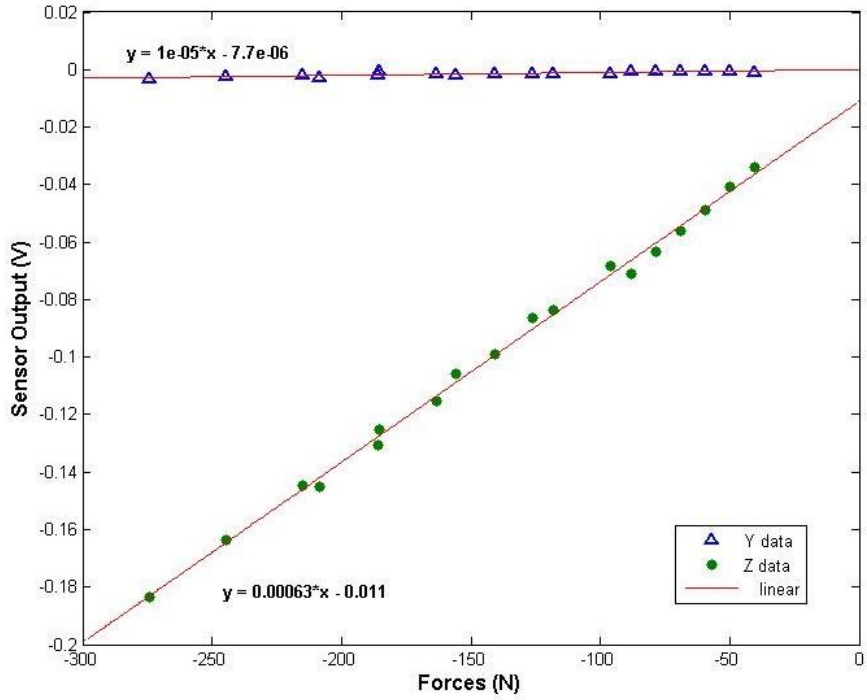

Figure 25: Sensor 1 Z-Axis Calibration

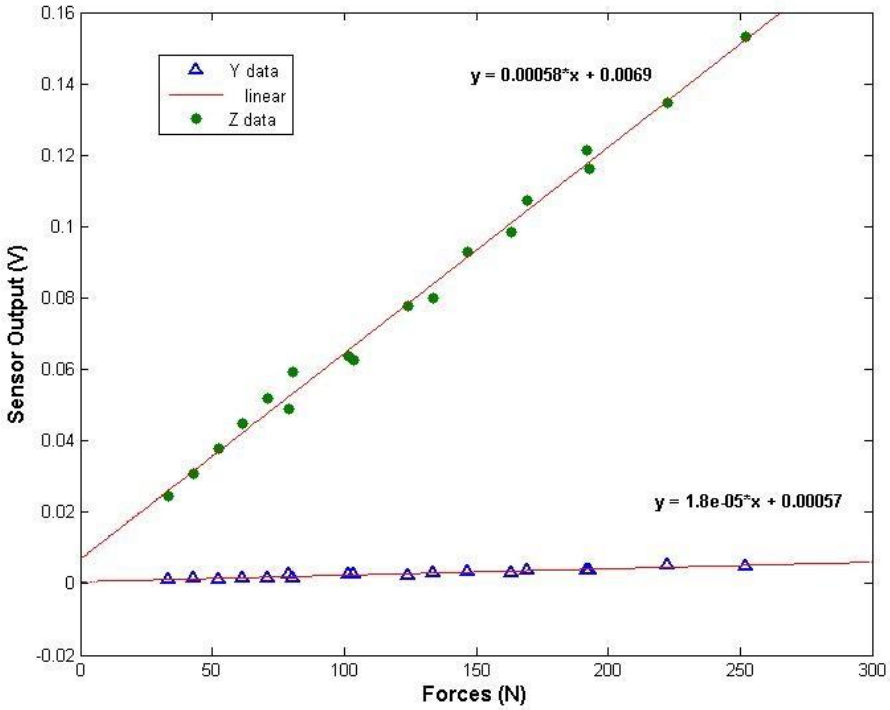

Figure 26: Sensor 2 Z-Axis Calibration

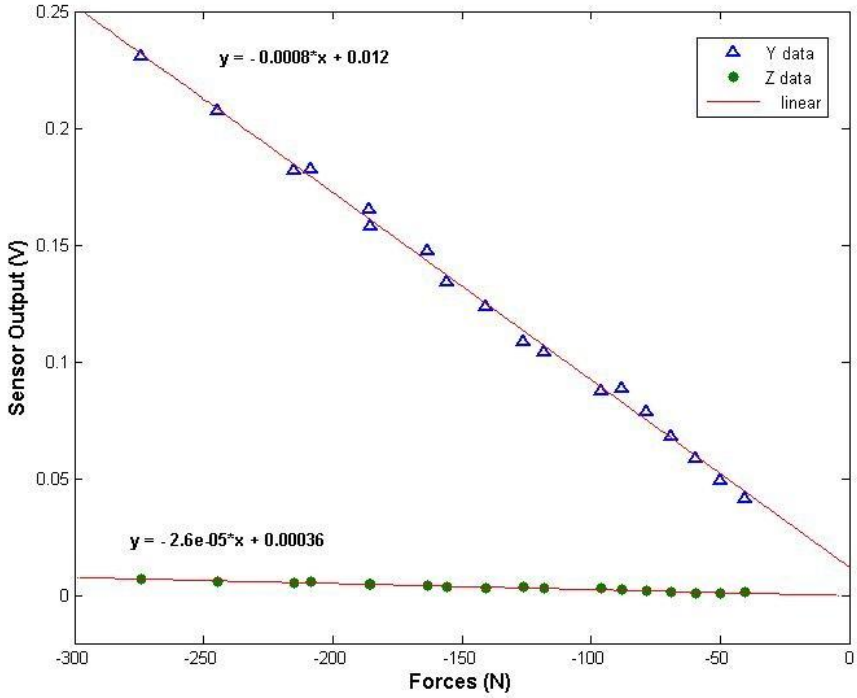

Figure 27: Sensor 1 Y-Axis Calibration

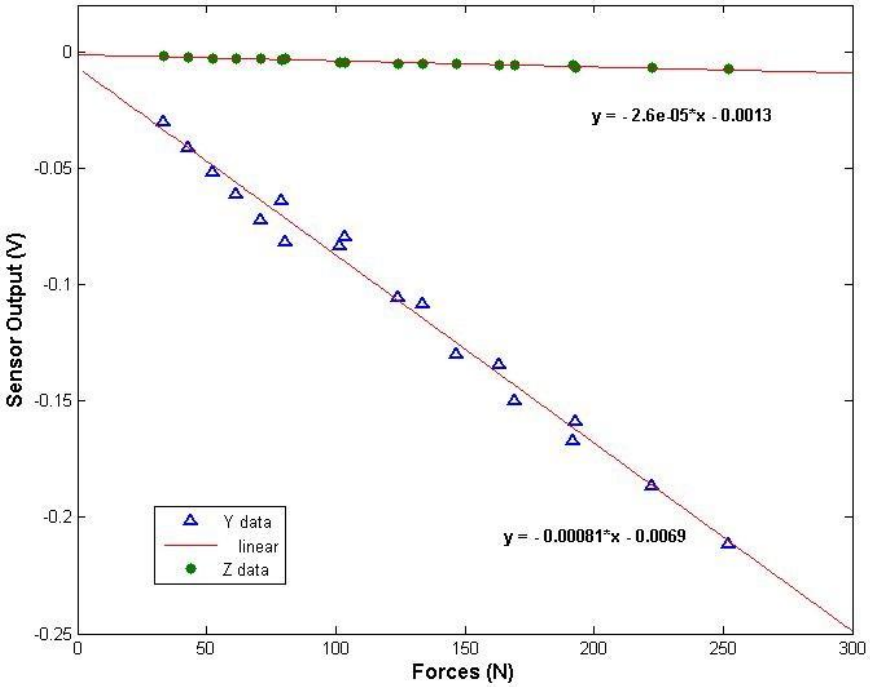

Figure 28: Sensor 2 Y-Axis Calibration

The figures 25-28 show linear fit quality and coefficients between measured voltages at both sensors and the calculated Y and Z forces. Nominally pure Y and Z forces were applied, allowing a linear fit to be found directly between the voltages and forces of the Y and Z axis for each sensor. Each plot shows evidence that a separate slope exists for the data points from each of the three weights hung. These slopes may be a result of the testing apparatus or sensor installation. They could also likely be an effect of the moment applied by system components, but they will be further explored in future work. The possible presence of a small amount of cross-sensitivity between each axis on both sensors can be seen, but it is not possible to separate this effect from error caused by the angle of the fin while weights were hung. Therefore, the cross-sensitivities were neglected. The slopes of the linear fit lines shown on each plot are the sensitivities (s) of the sensors in the indicated axes. Taking the inverse of these sensitivities gives the gain that is used with voltage measurements to find forces in the following equations.

$$f_Z^1 = (s_Z^1)^{-1} * V_Z^1 \qquad f_Z^2 = (s_Z^2)^{-1} * V_Z^2$$

$$f_Y^1 = (s_Y^1)^{-1} * V_Y^1 \qquad f_Y^2 = (s_Y^2)^{-1} * V_Y^2$$

From those equations, f denotes force, V denotes voltage measurement, the subscript letters correspond to sensor axes, and the superscript numbers state the sensor numbers. The sensitivities and gains are listed in the table below.

Table 2: Calibration Sensitivities and Gains

	$\boldsymbol{s_Z^1}$	$\boldsymbol{s_Z^2}$	$\boldsymbol{s_Y^1}$	$\boldsymbol{s_Y^2}$
From Plot Slope	.00063	.00058	-.00080	-.00081
Inverse Value (gain)	1587.3	1724.1	-1250.0	-1234.6

Calibration Error and Modifications

During calibration, human error could distort the readings based on hanging the weights, measuring the distances between them, and accurately aligning the fin angle. Furthermore, with more weights and more distances the total grid of measurements can be expanded which should increase the accuracy of calibration. The weights used could also be more precise too since the ones used are not from a standard set. Modifying the calibration method in these ways will increase the time it takes to calibrate, but if that becomes an issue the time could be reduced with an additional person helping during the procedure. There should not be any shortcuts taken during the calibration procedure as all data is essentially invalid without accurate calibration matrices.

4.2 Testing

The data from this project was collected to validate the test system by comparing to the results from past underwater flapping foil studies. The two sets of data for comparison come from the thesis discussing the design of the fin mechanics [Polidoro, 2003], and a paper looking at the performance of said fins [Techet, 2008]. Both ran experiments with a varying Strouhal number (St) and maximum angle of attack to find the mean thrust coefficient ($\overline{C_t}$) contours over the operational range of the fin at a specific heave to chord ratio ($\frac{h_0}{c}$). $\overline{C_t}$ values were compared to Techet, and instantaneous thrust and lift values were compared to Polidoro.

The tests run were almost exactly the same as those of Techet seen in Figure 2 with each red dot indicating a separate test run. To get enough data, the first four tests were run twice since their designated flapping frequency did not allow for ten or more

flaps per test. There was a minimum set of ten full strokes required for each combination of *St* and α_{max}. Therefore, there was a total of at least 32 tests run to create these results. The test matrix of those combinations is shown in Table 3.

Table 3: Test Matrix

Strouhal Number	***Maximum Angles Of Attack***
0.20	15, 20, 25
0.25	30
0.30	15, 20, 25, 30, 35
0.40	15, 20, 25, 30, 35, 40
0.50	15, 20, 25, 30, 35, 40, 45
0.60	20, 25, 30, 35, 40, 45

The full matrix with dimensional parameters is included in Appendix 4.

Analysis Process

There are four files created from each test run: (1) Force sensor no-load output voltage. (2) Force sensor, motor torque, motor velocity, and motor position during the run. (3) Position of the carriage from the LDM. (4) Force sensor no-load output voltage after each run. Each file is written as a .lvm file from LabView and are first parsed into organized matrices of force and position data using Matlab. The no-load output voltage files are then used to remove the static offset and linear drift of the force sensor measurements. Those measurements in volts are plotted so the useable data during the test can be chosen manually through graphical visualization. Voltages are then converted to estimated forces using the calibration matrices.

The forces acting at each sensor are used to calculate the moment about the roll and pitch axis. After a 5^{th} order Butterworth filter at 10 Hz is applied, the time sequence moment data is phase averaged using the peaks of the pitch motor position data as zero-phase. Throughout this process, the range of data collected, the carriage velocity, and thrust coefficients are all saved in external files. All of the programs used for analysis can be found in Appendix 2.

Sensor Forces to Fin Forces

The current distance between the force sensors do not allow for direct force measurement due to high noise production. Therefore, the forces must be calculated. The force values that come from each sensor are in opposite directions creating a moment about the perpendicular axis at the origin between them. Refer to the reference frame in Figure 4. Forces along the Z-axis produce a moment about the roll-axis while forces along the Y-axis produce a moment about the pitch-axis. The equations are as follows:

$$M_{Total} = (F_1 * d_1) + (F_2 * d_2)$$

Where M_{Total} is the total moment applied, F_1 and F_2 are the forces from sensors 1 and 2 respectively, and d_1 and d_2 are the distances from sensor 1 and sensor 2 to the axis of rotation which serve as the moment arms. The diagram in Figure 29 shows these forces and distances.

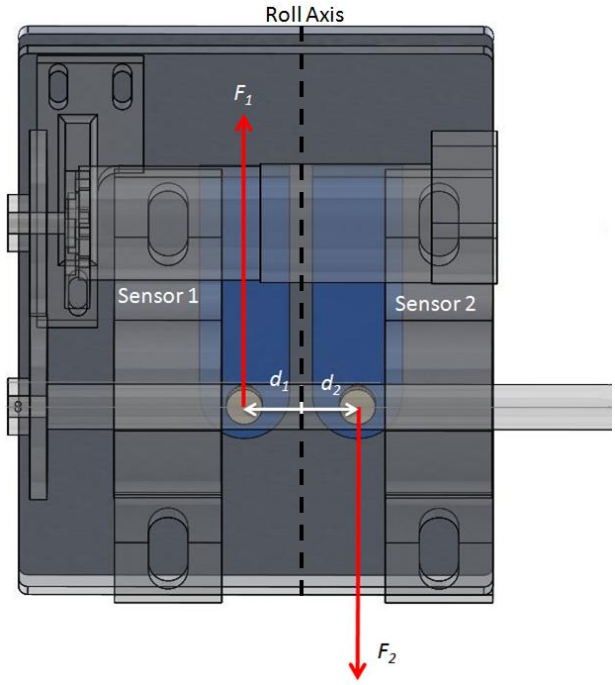

Figure 29: Forces Applied to Sensors

The forces applied to each sensor are typically a factor of ten larger than the force acting on the fin at the center of pressure location. The constant moment arms are always 1.5cm. The sum of these opposing applied moments largely cancels each other out. The resulting difference is the magnitude of the pure moment acting on that axis, which can then be converted to a force on the foil.

The calculated moments are divided by the distance to the center of pressure (d_{CoP}) to produce the forces at that point. Lift force (F_L) is determined from the Z-direction moment (M_Z) and thrust (F_T) is determined from the Y-direction moment (M_Y).

$$F_L = \frac{M_Z}{d_{CoP}}$$

$$F_T = \frac{M_Y}{d_{CoP}}$$

Thrust Coefficient Contours and d_{CoP} Assumption

For preliminary validation of the test system, the results were examined using an assumed d_{CoP} in the above formulas. To prove this method of assuming a d_{CoP} is credible, the following explains and shows how that assumption affects the results. The d_{CoP} is a linear factor which changes $\bar{C}_t$ contour values when modified, but the contour shapes remain the same. The d_{CoP} must be positioned between the root and the tip of the foil, which is a 0.4m range and extends from 0.155m to 0.555m from the roll axis. Therefore, there is a range of values that we can set as the d_{CoP}. To visualize the way $\bar{C}_t$ contours differ over this range, plots with the center of pressure located at the minimum, 70% of the span, and maximum distances are shown in figures 30-32.

$$\bar{C}_t = \frac{2\bar{F}_Y}{\rho U c S}$$

$\bar{C}_t$ was calculated via the formula above where $\bar{F}_Y$ is the mean thrust from phase-averaged thrust data. ρ is the water density, U is the fluid velocity, c is the chord length, and S is the span length.

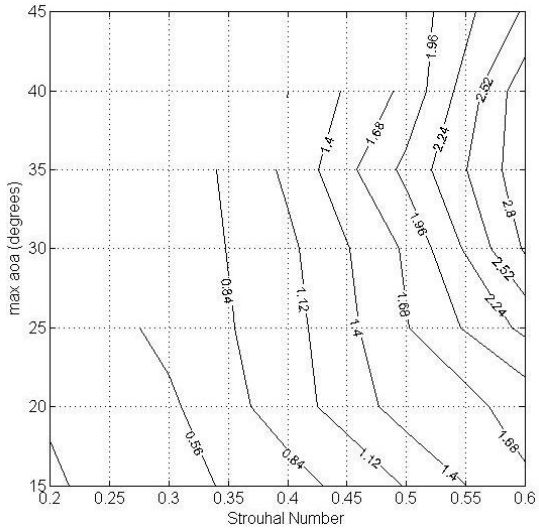

Figure 30: $\overline{C}_t$ Contour Plot CoP Minimum

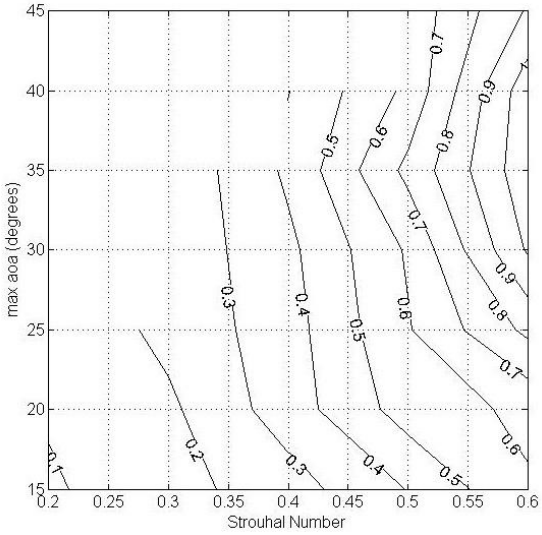

Figure 31: $\overline{C}_t$ Contour Plot CoP 70%

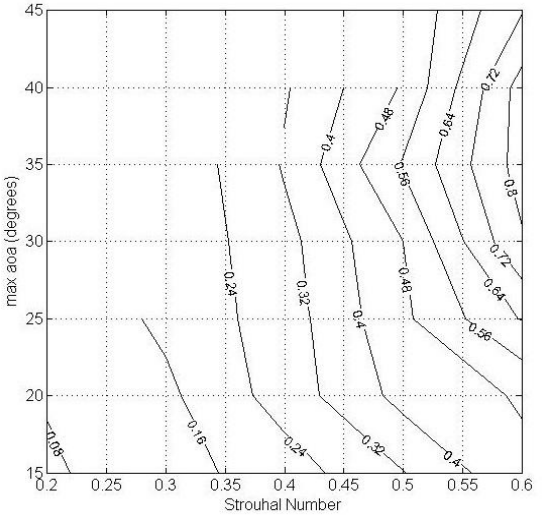

Figure 32: $\overline{C}_t$ Contour Plot CoP Maximum

The thrust coefficient contour plots all show similar patterns which helps to validate this test system when compared to the Techet data in Figure 2. It is evident from those results that thrust coefficients do not linearly increase with increasingly aggressive flapping. That is to say flapping foils do not generate peak thrust by flapping at the largest maximum angle of attack for a given Strouhal number. This pattern is evident in the curve of contours which create $\overline{C_t}$ peaks for each Strouhal number. Matching the general pattern of the prior contour plot gives a preliminary indication that this testing system will be able to recreate past data once the suggested modifications are implemented.

The assumed d_{CoP} values from root to tip of the foil show plots with maximum $\overline{C_t}$ that range from about 0.9 to 2.5. The past data in Figure 2 has a maximum of about 2.0, therefore a specific d_{CoP} can be linearly interpolated to produce contours with matching magnitudes. This distance is at 17% of the span length or 0.223 m from the roll-axis.

Figures 30-32, show the dependency of thrust generation on Strouhal number. Figure 33 is a plot generated with the same data as Figure 31, but with contours of lift amplitude coefficients (C_l). Lift amplitude is found by taking half of the summed maximum and minimum lift values. Therefore the formula for these coefficients is:

$$C_l = \frac{\frac{1}{2}\left(|\max(F_Z)| + |\min(Fz)| \right)}{\rho U c S}$$

Where F_Z is the phase averaged lift values, and the denominator is the same as in the $\overline{C_t}$ formula.

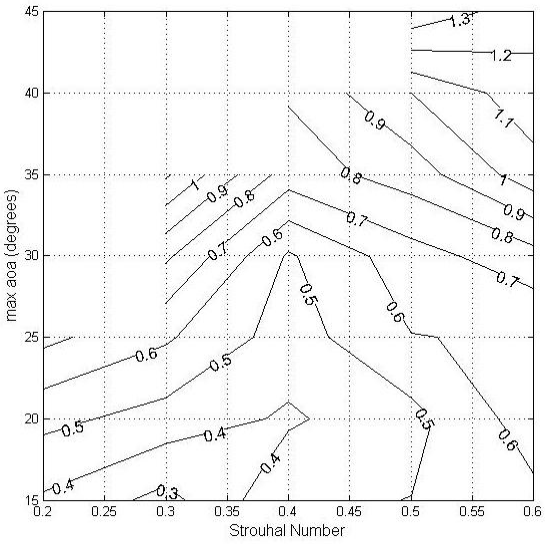

Figure 33: Cl Contour Plot

Figure 33 contours show that lift generation increases as maximum angle of attack increases. Thus, lift is dependent mostly on maximum angle of attack. This further illustrates the importance of the two parameters, Strouhal number and α_{max}, on flapping foils.

With data calculated using the interpolated 17% d_{CoP}, the instantaneous lift and thrust was plotted to compare to data taken in [Polidoro, 2003]. Significant differences exist between the test apparatus from that thesis and this present work. Testing was done with the foil piercing the surface of the water instead of being part of a fully submerged structure. The roll angle was varied in the past and kept constant for present testing. The ratio $\frac{h_0}{c}$ was 1.6 in Polidoro, while this project matched the $\frac{h_0}{c}$ ratio of Techet, at 1.5. The towing speed, span length, chord length, Strouhal number, and maximum angle of attack have all been matched. Below is the time sequence lift data from the two projects as Polidoro does not provide non-dimensional time data. The frequency difference is a function of the difference in roll angle used to achieve the same Strouhal number.

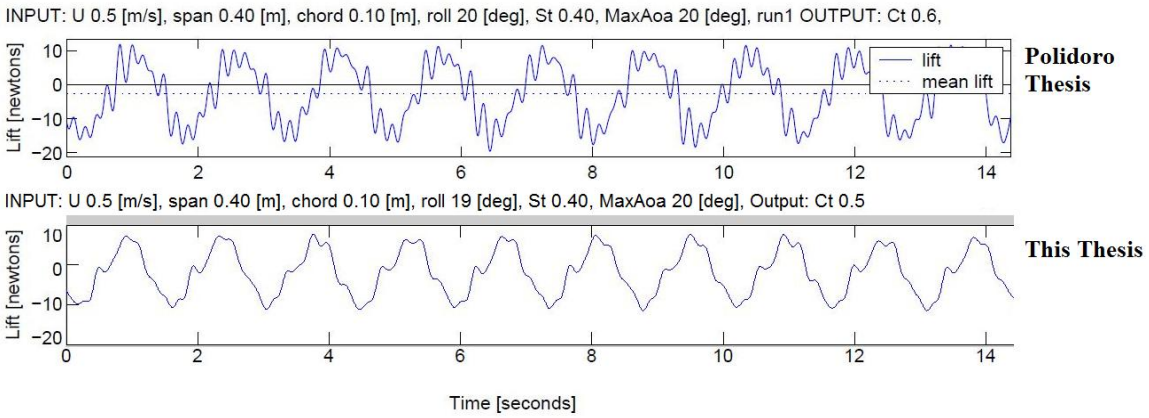

Figure 34: Polidoro Lift Comparison

The range of generated lift between the two theses is very close and the waveforms have similar anomalies. The average peak-to-peak magnitude from Polidoro, is 10N, as compared to 9N for this experiment with the 17% d_{CoP}. Each plot shows a pronounced "bump" on the slopes of each wave with the larger being on the side of the wave with a positive slope. Also, each plot shows larger negative peak magnitudes than positive peak magnitudes. That discrepancy should not exist and is likely caused by homing misalignment.

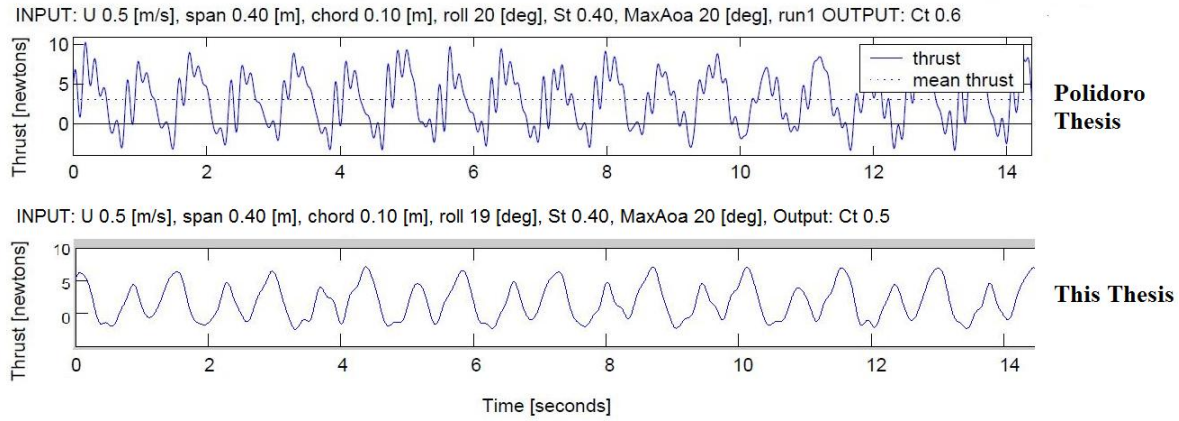

Figure 35: Polidoro Thrust Comparison

The figure above shows the same comparison as before but this time for thrust generation. The same discrepancies are evident in peak magnitude as well as frequency. For thrust, peak-to-peak magnitude from Polidoro is 8N as compared to 5N

from this experiment. Thrust is expected to be about twice the frequency of lift while being almost only positive. This is because thrust in a single direction is being produced on both upstroke and downstroke whereas lift is being produced in opposite directions on opposite strokes. The total lift-to-thrust ratio from Polidoro is 2.08, the total lift-to-thrust ratio from this thesis is 2.11. This comparison of ratios is compelling because it is unaffected by the d_{CoP}. Both plots adhere to theory, and it the approximate similarity between peak-to-peak magnitudes again show this test-system has the potential to recreate past data.

To further illustrate the relationship between generated lift and thrust, the figures 36-38 will show the phased averaged plots for three test runs characteristic of the full $\overline{C_t}$ measured range. This means that each wave of lift and thrust generated by the chosen test runs was averaged together over a single 360^o phase. The Strouhal number and α_{max} of each test are listed below the plots which can be matched the red dots indicating tests run on the contour plot in Figure 2.

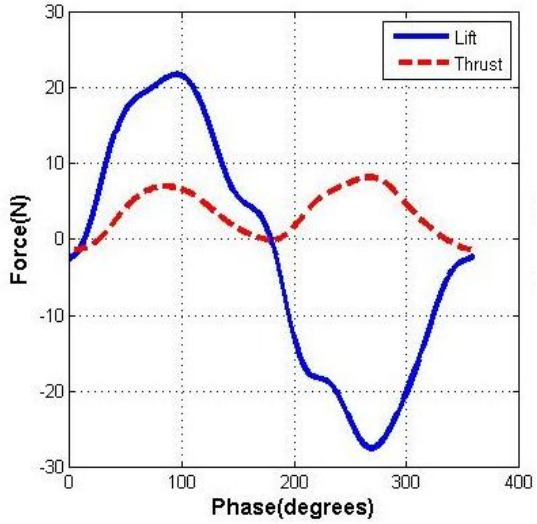

Figure 36: Phase Averaged Lift and Thrust at St = 0.4 α_{max} = 40° CoP = 17%

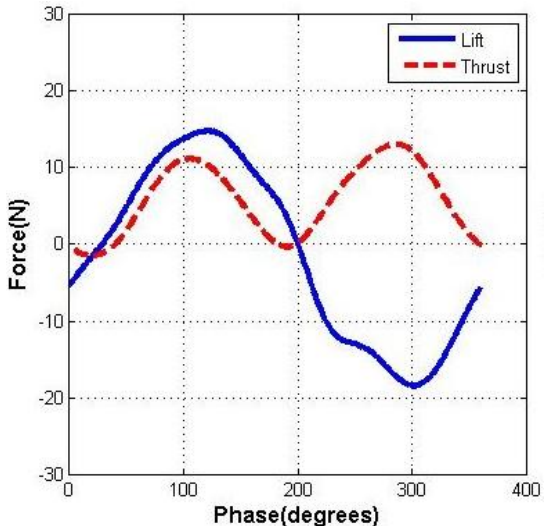

Figure 37: Phase Averaged Lift and Thrust St = 0.5 αmax = 30° CoP = 17%

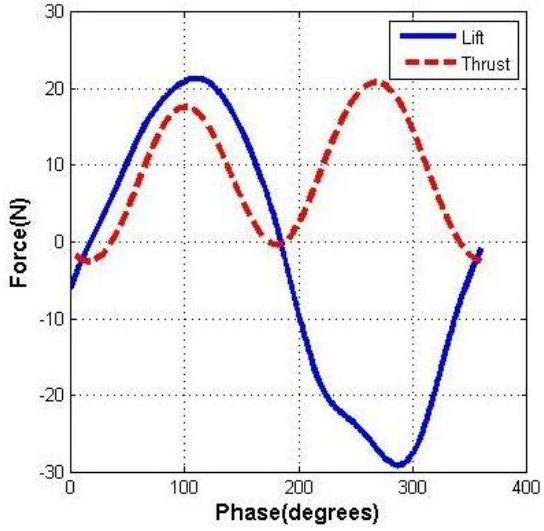

Figure 38: Phase Averaged Lift and Thrust St = 0.6 αmax = 30° CoP = 17%

All three plots above show the aforementioned relationship between lift and thrust. Peak lift magnitude is larger than peak thrust magnitude, thrust almost always positive, and thrust frequency is twice that of lift. There are three other trends that are evident in those plots. The first two have to do with the parameters chosen for each test, while the last is related to the testing setup.

The first of these trends is based on the relation between St and α_{max} of the flapping. St increases linearly from 0.4 to 0.5 up to 0.6 for each plot respectively, whereas α_{max} is 40^o for the top plot and 30^o for the bottom two. Lift generally increases with α_{max} as evidenced by the higher value in the first plot compared to the second. However, the bottom two rows share the same α_{max} so the differences in magnitude in those rows are based on the St difference which typically increases lift as well when increased. With a high α_{max} and low St value, Figure 36 produces very similar lift peaks to that of Figure 38 which instead used a lower α_{max} and high St value. The reasons behind this trend are that a higher α_{max} correlates to a larger pitch amplitude, and an increase in St means a frequency increase. Essentially, lift increases as the foil is flapping more aggressively.

The second trend of note is the thrust in relation to both St and α_{max} which is also clear in the $\overline{C_t}$ contour plots. Thrust increases and then tapers off through the α_{max} range. At $\alpha_{max} = 40^o$ the thrust peak magnitudes are much lower than those of lift even though this is relatively aggressive flapping. Conversely, thrust peak magnitudes are very close to those of lift when $\alpha_{max} = 30^o$ for both the 2nd and 3rd rows of plots. When both magnitudes are similar, the α_{max} is likely one of the values on the peak of the contour curves. That is, the α_{max} correlates to a max $\overline{C_t}$ for a given Strouhal number.

Thrust magnitude is increased with a St increase which is clear in the comparison of the all three plots. This is again attributed to more aggressive flapping.

The final trend is the discrepancy between downstroke and upstroke force generation. The first 180^o of each phase averaged plot shows the downstroke, or motion of the fin towards the tank bottom. The rest of each plot shows the upstroke. In all three plots, the magnitude of lift and thrust is greater on the upstroke than the downstroke, however they should be equal. This very likely happens due to a consistent homing offset before each test. With the fin starting at even a degree off in roll than the desired 0^o, the maximum roll angle would be a degree larger in one stroke and a degree smaller the opposite stroke.

CHAPTER 5

DESIGN IMPROVEMENTS AND ERROR ANALYSIS

Introduction

The force sensing system has a design flaw that produces unacceptable error in linear force measurements. Significant design changes are required to the pitch cylinder components for the system to perform correctly. With these modifications, the current tow-testing apparatus and analysis programs can still be used as they are for future experiments, though some adjustments could be made to increase repeatability.

Modifications Required for Accurate Linear Force Measurements

The current method of producing lift and thrust data, mentioned in the Methodology Section, using moments and assumed centers of pressure should not be necessary. The reason it was used is that there is too much noise in the force signals to accurately measure forces applied directly to the fin. This is likely caused by too little lateral distance between the sensors. Currently, the sensors are 3cm apart. That distance was caused by limited available space to install the sensors without having to heavily modify the organization of the pitch cylinder components. The force sensors should now be moved as far apart as possible (~12cm), an increase in distance by a factor of ~4. This should significantly reduce the signal to noise ratio by the same factor.

Another possible source of force measurement error comes from the sensors being bolted between two rigid plates. The forces on the fin are being translated

through the top plate to the sensors which could be applying a moment at the bolts as the plate is bent. The solution to this is to cut the plate in half and create a gap between the two halves such that applied forces to the new plate sections will not interact with each other. Similarly, moments could be applied during these tests by the two rigid pitch shaft bearings. To remove the ability for these bearings to apply moments, the rigid bearings will be replaced with spherical bearings.

Modifications for Better Repeatability

Another adjustment will be to change the location of the pitch shaft homing flag. The homing flag was originally set with the assumption that the fin could move through its full range of motion, and then the program could work from a known zero-position. For testing on this system and especially during experiments near a wall or bottom, the range of motion for the fin is constrained. However, the zero-position should be the same for every test and setting the homing flag to that new position with high accuracy and repeatable precision could eliminate the discrepancies in peak lift and thrust magnitudes shown in the data plots. This involves rotating the copper flag and tightening the collar that holds it so that it says fixed during testing. While homed though, the plane running through the center of the foil span lengthwise must be able to consistently reset parallel to the tank bottom. A more accurate 0^o reset would reduce the discrepancy between downstroke and upstroke force magnitudes.

Error Analysis

This tow-test system employs many instruments which all have factory quantified tolerances. Those tolerances certainly account for an important portion of the total error, though most cannot be improved and are likely negligible on the scale used for acceptable results.

Vibrations in the system likely cause significant noise in the force measurements. Much of this noise can be filtered out while still preserving the waveform, but there is no way to completely quantify or remove many of the vibration sources. The flapping foil is mounted to the bottom of the carriage attachment without any fairing for all testing in this thesis, but the profile is blunt enough that the pontoon setup could direct flow around the towing package with reduced noise. This will likely be tested during future experiments.

The carriage motor is very old a worn belt and gears which disrupts smooth carriage motion, this contributes to the inaccurate speed adjustment as described in the testing procedure section. The roll and pitch motor mechanisms can also add error like that of the carriage. The motors, encoders, gears, and belts have some tolerances and possible damage due to age. Specifically, the belts connecting the pitch motor to the pitch shaft are tightened by hand which means there could be some delay in what the motion controller tells the motor to do and what the actual motion of the foil is. These types of errors can be monitored and pieces can be replaced, but they can still account for anomalies that show up in the force output waveforms.

CHAPTER 6

FUTURE WORK

Introduction:

This future of this test system is focused on the ability to easily adapt and run new experiments. Due to the sources of error mentioned, and room for improvement, the testing setup can and will be modified. Ground-effect testing is set to be the first new experiments. Then, the effects changing the shape of fin in different ways will be examined. There is even research and designs for embedding pressure sensors in the molded fins. Each of these sets of experiments explores areas of research with little if any previous data.

Flapping Orientation

A change will be made to see if there is a noticeable difference between flapping oriented towards the wall (horizontal wall testing) compared to flapping oriented in the center of the tank (vertical wall testing). The latter, along with adding water to the tank is expected to further reduce the possibility of fluid boundary effects on the foil. To accomplish this, the flapping foil system is require

d to be rotated 180^{o} which means the masts will rotate similarly. While there should be no noticeable differences between the masts towed forwards or backwards, it is better to be consistent with the design. Of course, with the rotation of the masts and flapping foil, the carriage will now be moved in the opposite direction starting from the previous back of the tank and moving towards the beach. No extraneous issues should arise from this change other than taking caution not to actually hit the beach with the

submerged system during testing. Markings are already in place to indicate where the carriage can go, but future experiments may change the beach profile.

Ground-effect

The main purpose of this entire test-system is focused significantly on the ground-effect experiments. Ground-effect (GE) is a fluid flow phenomena created when airfoils are near a solid surface. The vortices formed under the airfoil compress instead of fully forming like those formed above the foil. This effect can produce increase lift, and decreased drag. GE occurs when $\frac{h_{ground}}{c}$ is less than 0.5 with h_{ground}being the height from the fin to ground, and c being the chord length. This means that sensing GE could indicate when a vehicle is near a solid surface, or could even allow the vehicle to utilize the benefits of GE in real time.

GE has been extensively researched as it relates to airplanes and helicopters. Russian *Ekranoplanes* are ground-effect airplanes that flew very close to lake surfaces while carrying much more weight with less necessary thrust power than a similar sized high altitude plane. The image below shows an Ekranoplane with rocket launchers on the top which would not be very aerodynamic, and very heavy. The cockpit in the picture can be used to scale the massive size of the plane further alluding to the extra available weight due to GE.

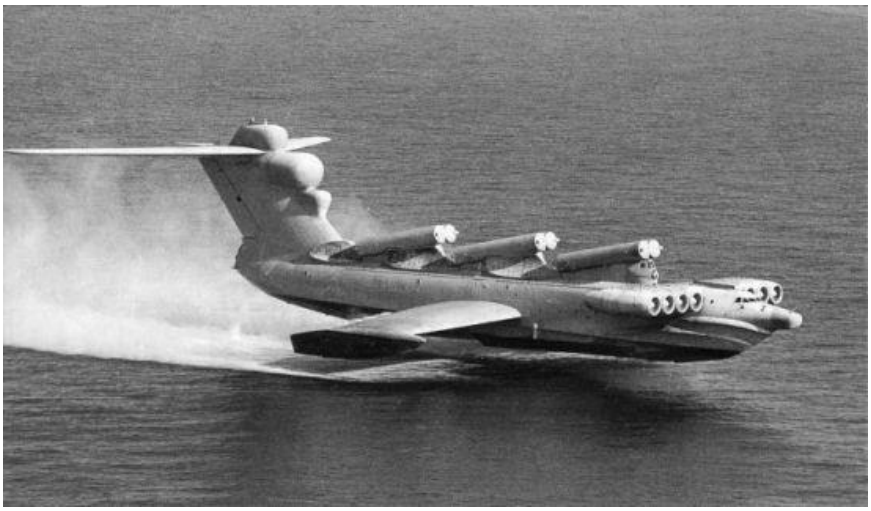

Figure 39: Russian Lun Ekranoplane
(http://www.aerospaceweb.org/question/aerodynamics/ground-effect/lun01.jpg)

Due to the rolling motion of the flapping foils, the fin will be moving alternatively closer to and farther from the flat surface (bottom of tow tank) during tests. Therefore, the hypothesis is that GE should only be visible on flapping foils when the stroke moves the foil into the aforementioned $0.5\ \frac{h_{ground}}{c}$ ratio. Also, the downstroke should have greater effects than the upstroke due to forcing vortices downwards towards the bottom.

Each set of ground-effect tests will be run with the flapping foil submerged at different distances from the bottom of the tank (h_{ground} from $\frac{h_{ground}}{c}$). The h_{ground} to begin with will be with the beach fully lowered as it is currently and without the cube spacer on the carriage attachment. This will be the open water test. The easiest depth adjusting is done by simply adding the cube spacer so that the h_{ground} is one span length lower than in the open water case. From there, the beach could be adjusted both with the cube on or off for finer yet more difficult h_{ground} tuning.

The goal of this testing will be to be able to detect ground-effect instantaneously without the need to compare to past data. This goal is a direct

reflection of a paper testing ground-effect on heaving and pitching foils [Licht & Dahl, 2013]. The ability to sense ground-effect on a test setup in a tow-tank with linear motion is significantly different from being able to do the same on a vehicle in a dynamic environment. Further research and testing would be necessary to differentiate ground-effect from other forces, and to develop a method to integrate this feedback with the vehicle controller.

Alternate Fins

There are multiple ways to change the fins used which can each produce thrust, lift, and efficiency results that could be used to enhance underwater flapping foil vehicles. The most significant changes would likely come from different planform shapes. From the introduction, the current fin design is shaped like a turtle fin. That planform has some advantages as it sheds tip vortices better than a rectangle would, but the chord changes so often which could result in lost thrust and lift. Therefore, tests can be done with shape from rectangles as a baseline up to more biological fin shapes for comparison.

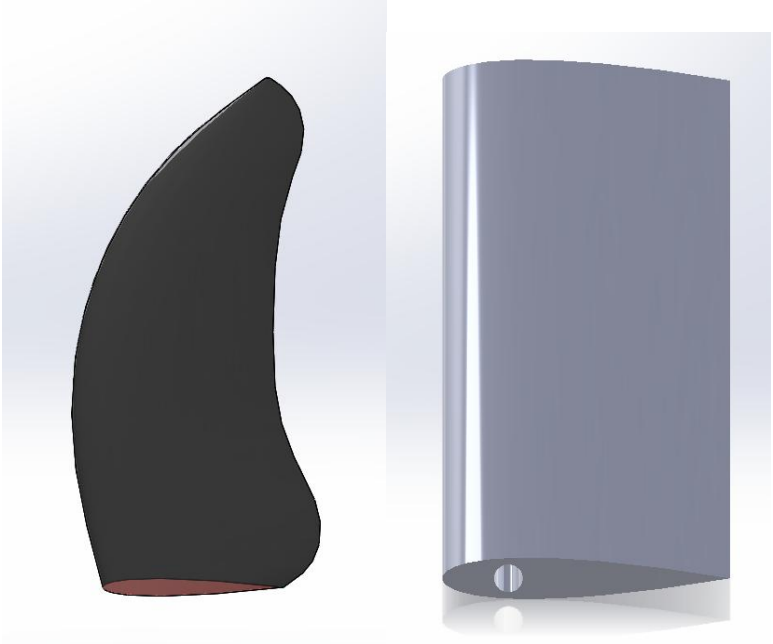

Figure 40: Different Planform Shapes

With the use of rectangular fins, the tip shapes can be changed from the flat 90^{o} edge to more rounded or pointed tips which keeps a constant chord length for much longer down the fin span, but also could show better methods to shed tip vortices.

The current fins were molded 5+ years ago and used enough to show regular wear and tear. The molded material is flexible, but molding a foil around the internal frame could have created air pockets and flexibility that varies instead of remaining constant. Therefore, the effects of changing the internal frame design and properties of the molding material could be tested on this system. The three main parameters that control the size of the fin are the span, chord, and airfoil used. Since the R-CUE lab is currently working on molding and 3-D printing new fins, they could be made with different aspect ratios. A higher aspect ratio achieves lift and thrust while minimizing losses due to tip vortices, however they would need more power to operate and more

space. Conversely a lower aspect ratio allows for more narrow and finer maneuverability while sacrificing the efficiency of the fin.

The current airfoil is a NACA 0012, but depending on the mission or vehicle operation environment other NACA foils could provide better results. Even adding some camber to the foil could be advantageous if the vehicle were to require very high lift in one direction. Having the ability to swap foils could give a single vehicle the ability to maneuver in a variety of environments or just enhance mission-specific operations.

Torque Sensor

A Kistler Type-9039 torque transducer similar in make to the force sensors will be installed on the pitch shaft to allow calculations of efficiency with those torque measurements. This sensor will be compressed between collars and spring washers to hold it in place and to be properly preloaded. The cable from this sensor will attach to a small amplifier mounted on the roof of the pitch cylinder. Since the sensor will be rotating with the pitch shaft, there needs to be a way to always know how far the shaft has rotated from starting position so the cable is not stretched tightly or unplugged. The communication cable receiving power and sending voltage measurements to the surface must be installed which means a new wet-mateable connector will have to be connected to include the necessary conductors and make sure to keep the pitch cylinder waterproof.

Embedded Pressure Sensors

The force sensors in the pitch cylinder are very useful in measuring the fluid forces acting on the foil as it flaps. However, they do not give any information regarding the fluid flow field over the foil. This can be done by embedding pressure

sensors in the foil either during or possibly after molding them. The idea is to create an array similar to the lateral line sensing of many fish. A method using the same analogy with just two pressure sensors was applied to a robotic fish [Ježov et. al. 2012]. In that case, they were measuring periodic vortices (pressure maxima) generated by fluid flow past a bluff body. They found increased swimming efficiency in synchronizing the flapping of the fin to the matrix generation period. Another study [Venturelli et. al. 2012], used 10-sensor arrays on two sides of a model fish and could distinguish between steady flow and Kármán vortex streets. Other students in the R-CUE lab already have extensively researched related literature, possible pressure sensors to use, and have designs on how to integrate them into the fins. Instantaneous pressure sensing like this could greatly improve obstacle avoidance capabilities.

CHAPTER 7

SUMMARY AND CONCLUSIONS

The goals of this thesis were to design, construct, test, and validate a system to research underwater flapping foils in a tow-tank. The design had to withstand large static and dynamic forces without being too cumbersome to operate efficiently. The materials were selected for corrosion resistance and to be streamlined while submerged in the tow-tank. Force sensors were installed in the pitch cylinder of the flapping foil, calibrated in-situ, and connected to the data acquisition system on the carriage platform. This data acquisition system was setup to record the force measurements, poll the motion controller of the flapping foil, record laser distance measurement, and then send it all via fiber-optic cable to computers. The files created by that data were processed and analyzed to produce the Results chapter.

A major assumption was made, the location of the center of pressure, in order to calculate the desired forces. The results were plotted to show the effect of this assumption and prove why the method produced credible results. Validation of this test system compared the newly generated data to that of past testing with these same fins. The mean thrust coefficient contours generated in this thesis match the curving pattern from Techet, 2008. Time sequenced lift and thrust forces display similar trends and waveforms compared to Polidoro, 2003. Phase averaged data adheres to expected theoretical results. Necessary improvements are being made on the foil and on the carriage attachment. Finally, with the enhancements implemented and the validation complete, the system will be fully operational to carry out the future experiments.

APPENDICES

APPENDIX 1: Kistler Type 9602 Specs

Force – FMT

KISTLER

Type 9602

FORCE SENSOR WITH INTEGRATED ELECTRONICS

Piezoelectric force sensor with integrated charge amplifier electronics for measuring and monitoring dynamic and quasistatic force components in industrial process measuring technology etc. in

- Metalworking machines
- Presses
- Forming machines
- Automatic assembly machines
- Transfer lines

- 1 or 3 force component versions
- Rugged, sealed case for use in harsh industrial environments (IP67 and IP68)
- Integrated charge amplifier electronics
- 2 electrically switched measuring ranges
- Available with plug-in or integrated cables
- Case optionally with straight or right-angled cable or plug outlet
- Various accessories

The sensor is suitable for indirect force measurements (force shunt mode) as well as for direct measurements in the main force flux. The force sensor produces an amplified, low-impedance force-proportional voltage signal which can be directly processed by machine control systems, for example. The sensor connection is made via a multipole cable which can be a plug-in or integrated type.

Type 9602... is supplied **uncalibrated.** For accurate measurement (absolute value)., the sensor must be calibrated in situ after installation.

Technical Data

		F_z	F_x, F_y
Measuring axes			
Measuring ranges			
Range I	kN	-5,0 ... 5,0	-2,5 ... 2,5
Range II	N	-1000 ...1000	-500 ... 500
Preloading	kN	25	–
Overload	%	20	20
Sensitivity (nominal)			
Range I	mV/N	≈1	≈2
Range II	mV/N	≈5	≈10
Linearity	%FSO	≤±1,5	
Hysteresis	%FSO	≤1,5	
Crosstalk			
$F_z \rightarrow F_x$, F_y	%	≈±3	
$F_x \leftrightarrow F_y$	%	≈±5	
F_x, $F_y \rightarrow F_z$	%	≈±3	
Rigidity			
c_z	N/µm	1250	
c_x, c_y	N/µm	240	
max. moment load (without simultaneous shear force load)			
M_z	Nm	-18/18	
M_x, M_y	Nm	-14/14	
Supply			
Voltage	V DC	11...30	
Current (1 channel)	mA	≈7	
Current (3 channel)	mA	≈11	
Output			
Voltage	V	±5	
Resistance	Ω	≈100	

Noise (0 ... 1 kHz)	mV_{pp}		<2
Offset	mV		<15
Time constant standard	s		long
Drift 0 ... 20 °C (typical)		F_z	F_x, F_y
Range I (pC/s <0,03)	mV/s	0 008	0,02
Range II (pC/s <0,03)	mV/s	0,04	0,1
Reset time	ms		<1
Reset Operate jump			
Range I (pC <2)	mV	<0,5	<1,25
Range II (pC <2)	mV	<2,5	<6,5
Control signal: Operate			
Reset Input open or	V DC		0 ... 1
Operate	V DC		3 ... 30
Control signal: Range			
Range I Input open or	V DC		6 ... 30
Range II	V DC		0 ... 1
Operating temperature range	°C		0 ... 60
Temperatur (min/max)	°C		-10/70
Vibration resistance (20 ... 200 Hz, cycle of 2 min, total 16 min)	g_{peak}		10
Shock resistance (1 ms)	g		200
Degree of protection (plug connection)	EN60529		IP67
Degree of protection (integr. cable)	EN60529		IP68
Cable protection			PUR
Weight (sensor only)	g		≈30

Kistler Instrumente AG, Postfach, CH-8408 Winterthur
Tel + 41 - 52 - 224 11 11, Fax 224 14 14, sales@kistler.ch, www.kistler.com

KISTLER

Block schematic diagram

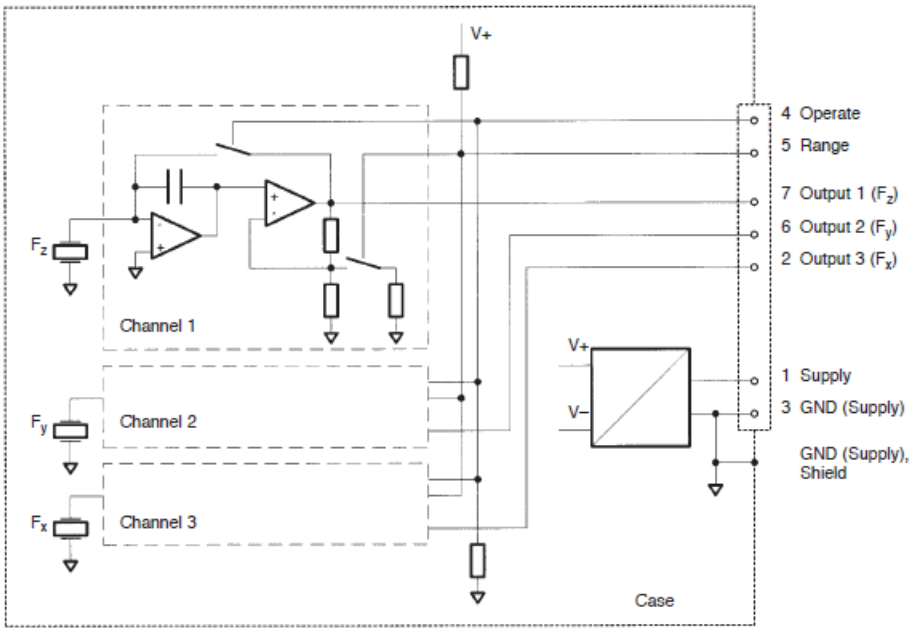

Accessories

- Preloading key Type 9463
- Connecting cable (to sensor with plug connection)
  Fischer SE102Z, ohne cable end unconnected
  Type 1783A5, l=5 m
  Type 1783Asp, special length (on request)
- Preloading disk with screw Type 9408
- Preloading set Type 9461

Sensor connector pin allocations

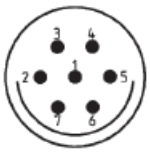

Pin	Color (open cable end)	Function
1	red	Supply
2	blue	Output 3 (F_x)
3	black	GND (signal)
4	green	Operate
5	orange	Range
6	gray	Output 2 (F_y)
7	white	Output 1 (F_z)
Screen		GND (Supply)

Sensor connection

For better interference signal rejection, we recommend the use of one differential amplifier per channel.

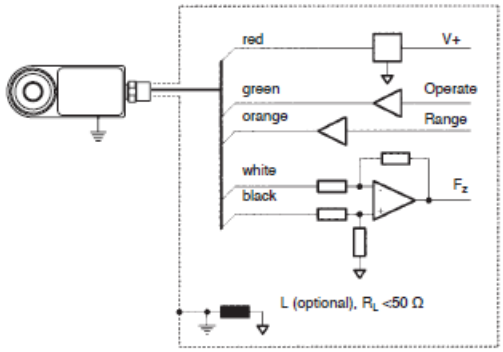

Electrical isolation can be achieved with one isolation amplifier per channel, two optocouplers for the control signals (Operate, Range) and an electrically isolated supply.

Kistler Instrumente AG, Postfach, CH-8408 Winterthur
Tel + 41 - 52 - 224 11 11, Fax 224 14 14, sales@kistler.ch, www.kistler.com

KISTLER

Dimensions

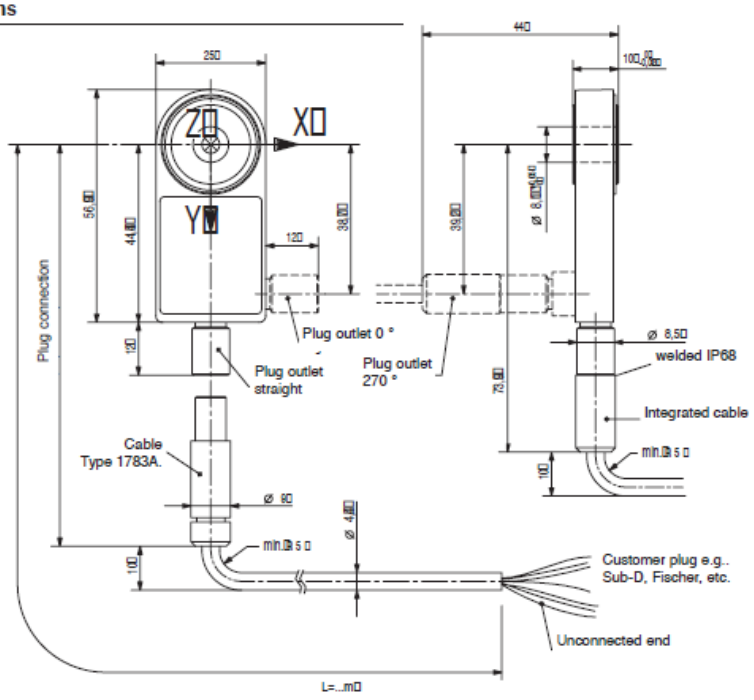

Mounting examples

Mounting (with preloading disk) between upper and lower parts of the structure.

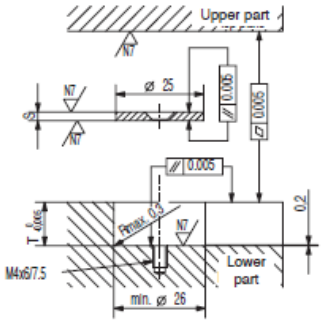

Fitting the sensor

1. Measure height H of the sensor
2. Measure depth T of the mounting bore.
3. Grind thickness S of the adaptation disk.
   Select S = (T-H) +0,015/+0,010, S ≥ 2 mm
4. Preload the sensor by assembling the base and cover plates.

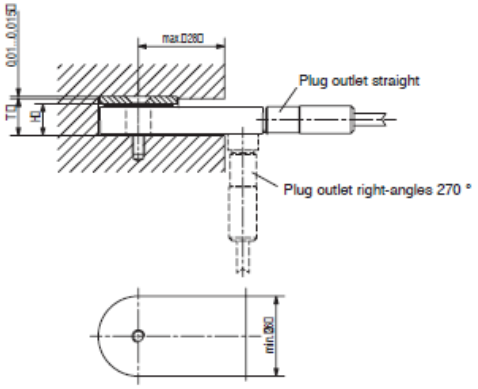

Kistler Instrumente AG, Postfach, CH-8408 Winterthur
Tel + 41 - 52 - 224 11 11, Fax 224 14 14, sales@kistler.ch, www.kistler.com

KISTLER

Mounting the sensor in machine structure with preloading disk Type 9463

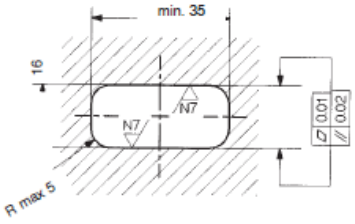

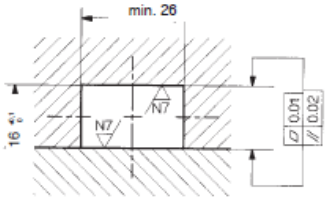

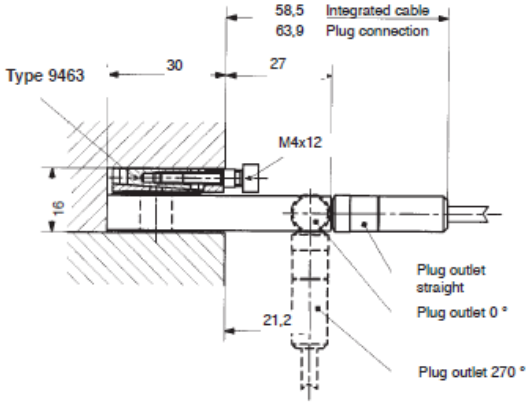

Fitting the sensor

1. Machine the mounting notch in the structure
2. Insert the sensor with preloading disk in the notch
3. Preload the sensor with the preloading disk

Mounting with preloading kit Type 9461 for direct force measurement

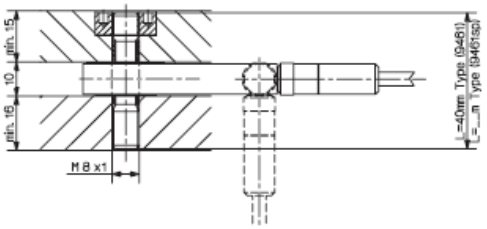

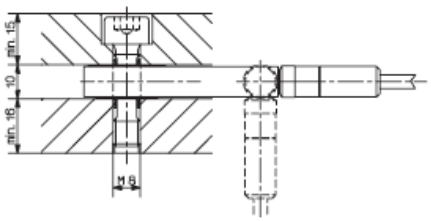

Ordering Code

Type 9602A□□□□

Measuring axes	
1-comp. (F_z)	1
3-comp. (F_x / F_y / F_z)	3
Sensor	
with plug connection	1
with integrated cable	2
Plug outlet at the sensor	
Straight	0
Right-angles, 0°	1
Right-angles, 270 °	2
Cable	
No cable (plug connection)	0
Integrated, l = 5 m	1
Integrated, special length	9

Kistler Instrumente AG, Postfach, CH-8408 Winterthur
Tel + 41 - 52 - 224 11 11, Fax 224 14 14, sales@kistler.ch, www.kistler.com

APPENDIX 2: Matlab Programs

Analysis0.m

```
%Sam Rauworth
%Use this script to fully parse, organize, and analyze data from
individual
%tests
%

close all
clear all
clc



addpath('429TM','425TM');
% rep = 'Y';
%
% while rep == 'Y'

%     hold off
filenm = input('Type test file name:   ','s'); %Change the name of
this file to the file that holds the data from the towed test

testnum = input('Input the test Number:   '); %Give the test a number
to associate with output data

[TVP, FSd] = DataParse0(filenm); %This function parses the data from
the above file
%TVP is Torque Velocity Position data from Control Card
%FSd is Force Sensor data

fileB =  input('Type ZB file name:   ','s'); %Change the file name
here for the beginning zero file of the chosen test.
fileE =  input('Type ZE file name:   ','s');%Change the file name
here for the ending zero file of the chosen test.
LDMfile = input('Type LDM file name:   ','s');
Vavg = Vfun0(LDMfile,testnum); %Change the file name here for the
laser range data to find average velocity of the test.
%User is asked to choose range of velocity to average

FSdz = zeroing0(FSd,fileB,fileE); %Finds the Force Sensor data after
zeroing it.

[FMd, TVPd, F1d, F2d] = Parse2FM0(FSdz, TVP,testnum); %Finds the
Force and Moments outputted by the force sensors.
%User is asked to choose the data range which is output to
Test_Range.txt
%FMd is the Force Moment data
%TVPd is the TVP data corresponding to the chosen FMd
```

```
FMdy = FMd(:,2);
FMdz = FMd(:,3);

[y,z] = BFilt0(FMdy,FMdz);


ztorque = (F1d(:,3)*(0.015))+(F2d(:,3)*(-0.015));
ytorque = (F1d(:,2)*(0.015))+(F2d(:,2)*(-0.015));
[Ty,Tz] = BFilt0(ytorque,ztorque);



time = (FMd(:,1)); %Time used with forces and moments (different
frequency than control card)
time2 = (TVPd(:,1)); %Time used with TVP (different frequency than
force sensors


[PhasedTz, LMz, UMz] = PhaseAvg0(TVPd(:,6), Tz, time2, time); %Can
change variable name and 2nd function input to phase average
different variables
[PhasedTy, LMy, UMy] = PhaseAvg0(TVPd(:,6), Ty, time2, time);

Lift = PhasedTz/0.155; %Converts phase averaged torques into forces
by dividing out moment arm or distance from axis of rotation to
center of pressure
Thrust = PhasedTy/0.155;%Min CoP is .155m, max is .555m, 70 percent
is .435m

for i = 1:length(Thrust)
    if isnan(Thrust(i)) == 0
        Thrust2(i,1)=Thrust(i);
    end
end

for i = 1:length(Lift)
    if isnan(Lift(i)) == 0
        Lift2(i,1)=Lift(i);
    end
end


Ct = (2*mean(abs(Thrust2)))/(1000*(Vavg^2)*.1*.4);
fid = fopen('Ctdata25p.txt','a');

fprintf(fid,'Test Number %f Ct %3f \n',testnum,Ct);

fclose(fid);
```

```
Ct = Ctfind0(filenm, fileB, fileE, Vavg, testnum); %Finds thrust
coefficient of phase averaged data and outputs to Ctdata.txt
%Currently re-does data range choosing and some other above functions


s = 360/(length(Lift2)-1);
r = 0:s:360; %s and r are arbitrary variables used to plot over 0 to
2pi

figure

plot(r,Lift2,'linewidth',3)
hold on
plot(r,Thrust2,'r','linewidth',3)
legend('Lift','Thrust')
grid on
axis square
xlabel('Phase(degrees)','FontSize',12,'FontWeight','bold')
ylabel('Force(N)','FontSize',12,'FontWeight','bold')

% rep = input('Want to run data again? Y/N \n','s');
% if isempty(rep)
%     rep = 'Y';
% end

% end
```

aoatest0.m

```
close all
clear all
clc

f = 1.02;
omega = f*(2*pi());
r7 = .445;
phi0 = 19 *(pi()/180);
t = 0:.05:10;
theta0 =27*(pi()/180);
U = 0.5;
c = 0.1;
h7 = r7*phi0;
h7oc = h7/c


for i = 1:length(t)
    alpha(i) = -atan((omega*r7*phi0*cos(omega*t(i)))/U) +
theta0*cos(omega*t(i));
end

alphadeg = (alpha.*180)./pi();

St = (2*r7*phi0*f)/U
Re = (U*c)/(1.004*10^(-6));

plot(t,alphadeg);

maxaoa = max(alphadeg)


desh7oc = 1.5;
rollh7oc = (desh7oc*c)/(r7*(pi()/180))

desSt = .6;
freq = (desSt*U)/(2*r7*(round(rollh7oc)*pi()/180))
```

Bfilt0.m

```
function [ yout, zout ] = BFilt0( ydata, zdata)
%Moving Average Filter
%Filters force sensor data forwards and backwards with moving
average.


[b,a] = butter(5,0.10,'low');

x1 = ydata;
x2 = zdata;
```

```
yout = filtfilt(b,a,x1);
zout = filtfilt(b,a,x2);


end
```

CtContour.m

```
%Sam Rauworth
%Use this script to plot Thrust Coefficient Contours
%

close all
clear all
clc

load Ctp25
CtP = Ctp25;

Ct =
[CtP(1:3);(ones(4,1)*NaN);CtP(5:9);(ones(2,1)*NaN);CtP(10:15);NaN;CtP
(16:22);CtP(23:29)];
a = .2:.1:.6;
b = 15:5:45;
[X,Y] = meshgrid(a,b);

Ct2 = reshape(Ct,size(X));

[c,h]=contour(X,Y,Ct2,'k');
clabel(c,h)
xlabel('Strouhal Number')
ylabel('max aoa (degrees)')
grid on
axis square
title('Ct contour of ho/c = 1.5')
```

DataParse0.m

```
function [ parsedTVP, parsedFS ] = DataParse0( filename )
%Takes .dat files from LabView and parses the data


fid = fopen(filename);

data = textscan(fid, '%f%f%f%f%f%f%f%s', 'Delimiter',
'\b\t','headerlines',23);

stringdata = regexprep(data{1,8}, '-', ' -');
parsedFS = [cell2mat(data(1)) cell2mat(data(2)) cell2mat(data(3))...
    cell2mat(data(4)) cell2mat(data(5)) cell2mat(data(6))
cell2mat(data(7))];



x = 1;
y = 0;
parsing = [];

for i = 1:10:length(stringdata)

        temp = cell2mat(stringdata(i));
        st = ' ';
        if strncmpi(st,temp,1) == 1
            temp=temp(2:end);
        end


            old = temp;
            new = temp(1:length(temp)-7);
            temp = new;


        nums = str2num(temp);

        for j = 1:length(nums)
            parsing(x,j+1) = nums(j);
        end
        parsing(x,1) = y;

    x = x+1;
    y = y+0.05;

end

frewind(fid);

parsedTVP = parsing;

end
```

Parse2FM0.m

```
function [ FMdata, TVPdata2, F1data, F2data ] = Parse2FM0( FSdata,
TVPdata, num )
%Takes parsed force sensor data, user chooses good data from plot,
%Force/Moment data outputted in x, y, and z directions


% load S1CalMat
% load S2CalMat

% CmS1 = S1CalMat;
% CmS2 = S2CalMat;


load S1Cb
load S2Cb

CmS1 = S1Cb;
CmS2 = S2Cb;

time = FSdata(:,1);

plot (FSdata(:,6))
[x,y] = ginput(2);
data (1,1) = round(x(1));
data (1,2) = round(x(2));

fid = fopen('TestRange25p.txt','a');

fprintf(fid,'Test Number %f Flag1 %3f Flag2 %3f \n',num, data);

fclose(fid);


S1V = [FSdata(:,4) FSdata(:,6)]';
S1F = CmS1*S1V;
S2V = [FSdata(:,5) FSdata(:,7)]';
S2F = CmS2*S2V;




m = data(1);
n = data(2);

for i = m:m+10
    if mod(i,10) == 0
        g = i;
    end
end
f1 = (g/10);
b1 = (f1*10)-9;
```

```
for j = n:n+10
    if mod(j,10) == 0
        h = j;
    end
end
f2 = (h/10);
b2 = (f2*10)-9;

TVPdatanew = TVPdata(f1:f2,2:7);
TVPtimenew = 0:.05:(length(TVPdatanew)/20)-.05;

TVPdata2 = [TVPtimenew', TVPdatanew];

FS1 = S1F(:,b1:b2);
FS2 = S2F(:,b1:b2);
FS = FS1+FS2;


time2 = 0:.005:((length(FS1))/200)-.005;


FMdata = [time2', FS'];
F1data = [time2', FS1'];
F2data = [time2', FS2'];

end
```

PhaseAvg0.m

```
function [ FMphased, Low, Up ] = PhaseAvg0( pdata, FMdata,
timep,timeFM )
%Phase averages FMdata over one 2pi cycle
%
 pdata = pdata+5200;

 [zc, ups] = zcross0(pdata,timep);
 [zc2, ups2] = zcross0(FMdata,timeFM);


 [ppy, ppx] = findpeaks(pdata);

col = length(ppx);


for j = 1:col-1;

    times(1,j) = timep(ppx(j));
    times(2,j) = timep(ppx(j+1)+1);

end

row2 = 0;



for k = 1:col-1

        for m = 1:length(timeFM)
            if (timeFM(m)>= (times(1,k))-.004 &&
timeFM(m)<=(times(1,k))+.004)
                times(1,k) = m;
            end

            if (timeFM(m)>= (times(2,k))-.004 &&
timeFM(m)<=(times(2,k))+.004)
                times(2,k) = m;
            end
        end
end

for i = 1:col-1

    temp = times(2,i)-times(1,i);

    if temp > row2
        row2 = temp;
    end
end
```

```
waves = NaN*(ones(row2+20,col-1));


for l = 1:col-1
    waves(1:(times(2,l)-times(1,l)),l) =
FMdata((times(1,l):times(2,l)-1),1);
end

if isnan(waves(1,end)) > 0
waves = waves(:,1:end-1);
end

for n = 1:length(waves)
    FMphased(n,1) = mean(waves(n,:));
    Low(n,1) = min(waves(n,:));
    Up(n,1) = max(waves(n,:));
end
end
```

Vfun0.m

```
function [ Vavg ] = Vfun0( filename, num )
%Takes .dat files from LabView and parses the data


fid = fopen(filename);

data = textscan(fid, '%f%f%s', 'Delimiter', '\b\t','headerlines',23);

for i=1:length(data{1,3})
    old = data{1,3}{i};
    new = old(1:7);
    data{1,3}{i} = new;
end

distances = str2double(data{1,3});

timing = data{1,1};

plot (timing, distances)
[x,y] = ginput(2);

flag1 = [x(1) y(1)];
flag2 = [x(2) y(2)];


Vavg = abs(flag2(1,2)-flag1(1,2))/(flag2(1,1)-flag1(1,1));

frewind(fid);


fid = fopen('Vavg.txt','a');

fprintf(fid,'Test Number %f Vavg %3f \n',num, Vavg);

fclose(fid);


end
```

APPENDIX 3: Testing Manual

Introduction

This Appendix section will explain the processes necessary to run tests, collect data, and analyze the data to form results. There have been significant improvements made to the apparatuses used as well as the collection and analysis programs while testing has been going. This means there could have been discrepancies between testing methods. These differences will be noted, and the corrections will be explained to show integrity of the data collected.

Testing Setup

Before putting the fin and carriage attachment (CA) in the water, it is important to check that all connections work, and that the pitch cylinder is watertight. Testing the connections just involves turning the DAQ Chassis power on and the 2-channel power source on, and then using the computer to run a simple motion while recording force sensor data. Once this is confirmed, a vacuum test is performed on the pitch cylinder. There is a bolt on the end of the cylinder that goes through the delrin into the interior. This bolt should be removed along with its o-ring, and the vacuum suction should be applied to the bolt hole. Once the vacuum reaches one atmosphere of pressure, and is turned off, the cylinder is watertight if the pressure does not change for an extended period of time. 5 to 10 minutes should be acceptable. Then, the bolt and o-ring can be replaced so the installation process can continue.

The installation of the CA with flapping foil has been outlined in the CA section, Chapter #. Once the structure has been bolted down, the wiring connections are fairly straight forward. The outputs from the force sensor Cat 5 cables connect to the labeled inputs for the I/O boards, and power and ground wires for the force sensors

and the foil are connected to their respective channels on the power source. The laser turns on automatically when the chassis gets power. Before the power source and DAQ chassis are turned on, the fin must be rotated to the upper roll limit with 0^o pitch. This positioning is the origin set as (0,0) by the control card which allows the user to set a desired starting position relative to the same origin for every test. With everything powered up, the computer on-land can then be turned on. If the computer is turned on prior to those steps, it may not recognize the carriage platform chassis. In Galil on the computer, for the testing in this project, the starting position of the fin from the origin mentioned is set using these commands:

$$PA\ -5200,0$$

$$BG$$

This means the absolute position of the fin (PA) relative to (0,0) is -5200 counts of the roll motor, and no change in the pitch. BG begins the motion. It is always good to constantly check the position of fin whenever attempting to return to this point. Resetting after each test should be close to -5200,0 using the command TP for tell position. However, since there are 50,000 counts in the roll motor and 102,000 counts in the pitch motor, the difference in position can vary by up to 100 counts without even being off by a single degree so some leeway is granted.

Presumably, the setup so far has been done with the carriage in a position other than the correct starting position, so the next step is to move the carriage there. This is done using the carriage motor controller with switches for direction, starting and stopping the motor, and a potentiometer that regulates carriage speed. The starting position doesn't always have to be the same, and is based on the depth of the fin

compared to the bottom, as well as the desired test travel distance. The travel distance can be calculated on a per-test basis in the equation below by using the flapping frequency, carriage velocity, and desired number of flaps.

$$Distance\ (m) = \frac{Desired\ Number\ of\ Flaps(Fl) * Carriage\ Velocity\ (\frac{m}{s})}{Flapping\ Frequency\ (\frac{Fl}{s})}$$

There are taped markings along the rim of the tow-tank that indicate 1.5 meter sections to be used for positioning and timing. As mentioned in chapter #, the velocity is constant through each test and therefore can be found with the time it takes for the carriage to travel between two known points. Currently, this is done using the LDM 42, but previously it has been timed using a stopwatch and visually watching the carriage pass those markings. Tests were run multiple times to ensure consistent measurements with velocities varying by mere thousandths of a second per test.

Tow-Testing Process

When everything is ready to run a test, the program FSCollect is run in LabView to record force sensor output for 20 seconds. With no foil motion this provides a baseline (zero) as a reference to compare the same output from 20 seconds without motion at the end of the test. The force sensors have a linear drift which can be removed using these two zeroing files for each test. A benefit of running the zeroing program for 20 seconds before each test is it allows the water in the tank at least that amount of time to settle between each test and each carriage reset.

With the baseline zero data recorded, the foil motion is started using Galil Tools Lite (Galil), which is the proprietary program for the control card on the foil system. Control is done by setting a flapping frequency, a roll amplitude, and a pitch amplitude using the commands:

$$FR = (frequency\ value)$$

$$AMX = (roll\ amplitude\ in\ degrees)$$

$$AMY = -(pitch\ amplitude\ in\ degrees)$$

$$CHANGE = 1$$

Due to the direction of towing and the setup of this particular foil, the pitch amplitude is always set as a negative value in this project's testing. CHANGE = 1 is the command that applies the previous commands. With that done, the foil will start flapping, but Galil cannot stay open during data collection due to the collection program's need to take over connection to the foil system control card. So, with Galil closed, the program DataCollect is run in LabView. This program runs the same force sensor collecting and displaying as FSCollect, and it also polls the foil system control card for the motor torque (V), velocity (counts/s), and position (counts) at a rate of 1 polled measurement per 10 force sensor measurements. Testing has been done with the force sensors at 200hz and therefore the polling at 20hz. After DataCollect is started and connected to the foil, the program LDM is run simultaneously to for carriage velocity data. The carriage is then run for the experiment.

The carriage is controlled via the box shown in the image below. The direction switch is set first, the motor start button is depressed, and the velocity potentiometer is turned to the correct position at a calm pace. The carriage should accelerate to the desired constant velocity inside one 1.5 meter section. A hose clamp is connected to the potentiometer (as shown below) to set a maximum velocity limit at the desired test velocity. The excess length of the clamp hits the silver U-bolt to limit the turn of the potentiometer. This is currently the best option for velocity regulation, and the

position of the clamp is tested 3 times minimum to make sure it drives the carriage at a consistent velocity within a hundredth of a second variation. The carriage stops in a safely short distance so the stop button can be depressed at the end of the testing travel distance.

Figure 41: Carriage Motion Controller

After the carriage is stopped, any running programs are stopped as well. Then, upon reopening Galil, the roll and pitch amplitudes are set to 0 degrees thus resetting the fin position using commands:

$$AMX = 0$$

$$AMY = 0$$

$$CHANGE = 1$$

It is at this point the FSCollect program is run again for the 20 seconds of end zeroing data. Then, the carriage can be returned to the starting position. At the starting position, all the testing steps can be repeated starting from running FSCollect for the 20 seconds of starting zeroing data.

There is one parameter that is very important to check before each test. Resetting the fin to the home position is followed by a command "TP" that polls the motor controller for the position in counts from 0 that each motor is at. Clearly this value should be as close to if not exactly 0 every time, but they typically vary by up to

±50 counts on the pitch motor and up to ±20 counts on the roll motor. These variations are generally negligible since there are 102,000 total counts in pitch and 50,000 counts in roll. That means that a difference of hundreds, even a thousand counts in pitch would be required to alter homing by just 1^{o}. These values should always be monitored, but there should not be too much worry.

APPENDIX 4: Full Test Matrix

Test ID #	Flapping Frequency (Hz)	Roll Amplitude (^{o})	Pitch Amplitude (^{o})	Strouhal Number	Max Angle of Attack (^{o})
1	0.34	19	17	0.2	15
2	0.34	19	12	0.2	20
3	0.34	19	7	0.2	25
4	0.42	19	7	0.25	30
5	0.51	19	28	0.3	15
6	0.51	19	23	0.3	20
7	0.51	19	18	0.3	25
8	0.51	19	13	0.3	30
9	0.51	19	8	0.3	35
10	0.68	19	38	0.4	15
11	0.68	19	32	0.4	20
12	0.68	19	27	0.4	25
13	0.68	19	22	0.4	30
14	0.68	19	17	0.4	35
15	0.68	19	12	0.4	40
16	0.85	19	47	0.5	15
17	0.85	19	40	0.5	20
18	0.85	19	33	0.5	25
19	0.85	19	28	0.5	30
20	0.85	19	23	0.5	35
21	0.85	19	18	0.5	40
22	0.85	19	13	0.5	45
23	1.02	19	48	0.6	20
24	1.02	19	40	0.6	25
25	1.02	19	33	0.6	30
26	1.02	19	27	0.6	35
27	1.02	19	22	0.6	40
28	1.02	19	17	0.6	45

BIBLIOGRAPHY

Jezov, Jaas, Otar Akanyeti, Lily D. Chambers, and Maarja Kruusmaa. "Sensing Oscillations in Unsteady Flow for Better Robotic Swimming Efficiency." *Proc. of 2012 IEEE International Conference on Systems, Man, and Cybernetics,* South Korea, Seoul.

Jones, Kevin D., and Max F. Platzer. "Design and Development Considerations for Biologically Inspired Flapping-wing Micro Air Vehicles."*Experiments in Fluids* 46.5 (2009): 799-810. Web. 5 Apr. 2014.

Lagor, Francis D., Levi D. DeVries, Kathryn M. Waychoff, and Derek A. Paley. *Bio-Inspired Sensing and Control: Autonomous Underwater Navigation Using Distributed Pressure Measurements*. Proc. of UUST, New Hampshire, Portsmouth. Print.

Lee, Sang-Hwan, and Juhee Lee. "Aerodynamic Analysis and Multi-objective Optimization of Wings in Ground-effect." *Ocean Engineering* 68 (2013): 1-13. *ScienceDirect*. Web. 25 June 2013.

Licht, Stephen Carl. "Biomimetic Oscillating Foil Propulsion to Enhance Underwater Vehicle Agility and Maneuverability." Thesis. Massachusetts Institute of Technology and Woods Hole Oceanographic Institution, 2008. Print.

Licht, Stephen, and Jason Dahl. "Thrust and lift generation in 'ground-effect' for heaving and pitching high aspect ratio foils." *2013 UUST Conference*, Portsmouth, NH.

Park, Kyoungwoo, and Juhee Lee. "Optimal Design of Two-dimensional Wings in Ground-effect Using Multi-objective Genetic Algorithm." *Ocean Engineering* 37 (2010): 902-12. *ScienceDirect*. Web. 25 June 2013.

Polidoro, Victor. "Flapping Foil Propulsion for Cruising and Hovering Autonomous Underwater Vehicles." Thesis. Massachusetts Institute of Technology, 2003.

Quinn, D. B., and A. J. Smits. "Rectangular Panels Undergoing Pitch Oscillation in Ground-effect." *1000 Islands Fluid Mechanics Meeting* (2012): Print

Techet, A. H. "Propulsive Performance of Biologically Inspired Flapping Foils at High Reynolds Numbers." *Journal of Experimental Biology*211.2 (2008): 274-79.

Truong, Tien Van et al. "Flow Structures around a Flapping Wing considering Ground-effect."*Experiments in Fluids* 54.1575 (2013): 1-19. Print.

Venturelli, Roberto et al. "Hydrodynamic Pressure Sensing with an Artificial Lateral Line in Steady and Unsteady Flows." *Bioinspiration & Biomimetics* 7 (2012): 1-12